Progress in Oceanography 217 (2023) 103076

Contents lists available at ScienceDirect

Progress in Oceanography

journal homepage: www.elsevier.com/locate/pocean

Seasonality and drivers of water column optical properties on the northwestern Barents Sea shelf

Håkon Sandven [a,b,*], Børge Hamre [b], Tristan Petit [a,b], Rüdiger Röttgers [c], Hongbo Liu [b], Mats A. Granskog [a]

[a] Norwegian Polar Institute, Fram Centre, Tromsø, Norway
[b] Department of Physics and Technology, University of Bergen, Bergen, Norway
[c] Institute of Carbon Cycles, Helmholtz-Zentrum Hereon, Geesthacht, Germany

ARTICLE INFO

Keywords:
Optics
Barents sea
Seasonal changes
Phytoplankton
Suspended particulate matter
Under-ice blooms

ABSTRACT

Hydrographic and bio-optical measurements were conducted along a south–north transect on the northwestern Barents Sea shelf from early spring to late summer in 2021. Strong climate change manifestations observed in this region are rapidly changing the marine environment. These rare observations cover the seasonal evolution from well-mixed and sea ice-covered winter conditions, through sea ice retreat in spring, to late summer where the sea ice had largely retreated and the water column was stratified due to sea ice melt.

Phytoplankton drives the spatial and temporal variability in optical properties in most of the water column, but increased scattering and absorption could also be seen in the bottom boundary layer due to resuspended particles. The relationship between chlorophyll-a and particulate absorption deviates from the globally observed relationship, likely due to light adaptations in the ice-covered water masses. We recommend developing specific models for spring phytoplankton growth in ice-covered waters to accurately account for self-shading effects. The absorption of colored dissolved organic matter (CDOM) was relatively low, due to waters of Atlantic origin in the studied region, and varied considerably less than particulate absorption. CDOM was nevertheless the optically dominant ocean constituent in the very clear waters in late winter.

Regional relationships for estimating particulate organic carbon (POC) and chlorophyll-a concentrations from *in situ* attenuation and fluorescence measurements were developed. POC may act as an alternative indicator to chlorophyll-a for optical properties in ice-covered open ocean, which is relevant for light availability parametrizations in biogeochemical ocean models.

1. Introduction

The primary producers of the ocean require light for photosynthesis. Light is therefore an key environmental factor in marine ecosystems, especially at high latitudes, yet remains difficult to model and measure accurately (Castellani et al., 2022). While the theoretical limit for photosynthesis is estimated to be 0.01 μmol photons/m^2 s (Raven et al., 2000), the operational limit for the compensation irradiance has been found to be approximately 4–15 μmol photons/m^2 s (diurnal average of 0.35–1.3 mol photons/m^2 day) depending on species or physiological state (Siegel et al., 2002; Ardyna et al., 2020), which is comparable to light levels in a dimly lit room. The compensation irradiance is the light level at which gains through primary production are balanced by losses due to processes like grazing, sinking and respiration. This limits photosynthesis to surface waters throughout the global ocean, and restricts primary production below thick sea ice or during the polar night in high-latitude Arctic waters. During the polar night, phytoplankton goes into a hibernation-like state, and remain ready to rapidly respond to an increase in light availability (Hoppe, 2022). In the ice-covered Arctic, sea ice algae are another key primary producer (e.g. Gosselin et al., 1997; Leu et al., 2015). Kelp and other benthic plankton in shallow coastal waters are also influenced by sunlight (Bartsch et al., 2016; Castro de la Guardia et al., 2023), as well as many higher trophic-level organisms throughout the ocean (Kaartvedt et al., 2019; Omand et al., 2021). Most fish are visual feeders, meaning that predator–prey dynamics between zooplankton and fish often results in diel cycles following the available sunlight at depth (Häfker et al., 2022), and even responds to moonlight during the polar night (Cohen et al., 2015).

In the past, primary production has often been assumed to be negligible in strongly ice-covered waters due to light-limitation (with the exception of the marginal ice zone), but an increased effort to observe

* Corresponding author at: Department of Physics and Technology, University of Bergen, Bergen, Norway.
E-mail address: hakon.sandven@uib.no (H. Sandven).

https://doi.org/10.1016/j.pocean.2023.103076

Available online 21 June 2023

phytoplankton within and below sea ice in the past 15 years have changed our perspective (Leu et al., 2015; Assmy et al., 2017; Ardyna et al., 2020). Enough light to support photosynthesis can frequently be transmitted through melt ponds or leads in the ice, enabling surface blooms. Significant thinning of the Arctic sea ice around 2007 has likely enhanced this process (Sumata et al., 2023; Nicolaus et al., 2012), but snow and cloud cover also play strong yet poorly constrained roles in the underwater light availability (Bélanger et al., 2013; Omand et al., 2021; Hamre et al., 2004). Stratification caused by melting sea ice may often act as a trigger for spring blooms, but can also inhibit carbon sequestration from surface waters (von Appen et al., 2021). By contrast, ice formation in the autumn and winter has been found to be a significant driver of lateral transport of organic carbon from productive shelf areas in the north-eastern Barents Sea (Rogge et al., 2023).

The changing Barents Sea and Arctic Ocean

The Barents Sea is a shelf sea adjacent to the European Arctic Ocean, and is one of the most rapidly warming regions on the planet due to anthropogenic climate change, with up to 2.7 °C increase in air temperature per decade observed for northern Barents Sea (Isaksen et al., 2022). The entire Arctic region has warmed on average four times as fast as the global average in the past decades (Rantanen et al., 2022). Observations also show a rapidly decreasing sea ice cover in the Barents Sea, and the area is projected to become largely ice-free towards the end of this century (Onarheim and Årthun, 2017). Increased *Atlantification* is bringing in saltier and warmer waters into the region, and the *Polar Front*, forming the boundary between Atlantic and polar water masses, is moving northwards and eastwards in the Barents Sea (Ingvaldsen et al., 2021). This process is accelerating sea ice melt, which increases light availability and wind-driven circulation in the surface layer, but also results in increased stratification and thus more nutrient-limitation (Oziel et al., 2017; Wassmann et al., 2006). However, stratification in the Barents Sea is largely due to sea ice melt, and decreased sea ice melt has made the water column less stratified in some years due to lower sea ice import (Lind et al., 2018). Looking at a longer time horizon, even the seasonal sea ice may eventually disappear completely in from the Barents Sea, and with it the sea ice melt-driven stratification. Consequently, the environmental framework for marine ecosystems in the Barents Sea is fundamentally changing. Increased light availability, due to thinner ice and longer open-water periods, is a key factor for changing marine ecosystems in the Arctic Ocean and the Barents Sea, in addition to the changing hydrography and nutrient dynamics. It is particularly challenging to estimate present and future light availability of the water column in the Arctic Ocean and the Barents Sea, as underwater light is governed by solar angle, cloud cover and a heterogeneous sea ice cover including snow (Castellani et al., 2022). However, the optical properties of the water column may also play a significant role (Pavlov et al., 2017).

Inherent optical properties

Phytoplankton are dependent on light, but light availability also depends on the concentration of phytoplankton and other suspended particulate and dissolved matter in the water column. Light propagation in water depend upon the absorption and scattering properties of the water masses, which are needed to model irradiance with depth using radiative transfer models. These *inherent optical properties* have been found to vary with ocean constituents such as phytoplankton concentration, particulate and dissolved matter, and have therefore been extensively studied for ocean color remote sensing applications in both the global ocean and coastal and inland waters (Bricaud et al., 1998; Werdell et al., 2018). Here, focus has been primarily on retrieving the ocean constituent concentrations. The volume light absorption coefficient $a(\lambda)$ is conventionally decomposed by

$$a(\lambda) = a_{\text{water}}(\lambda) + a_{\text{CDOM}}(\lambda) + a_{\text{ph}}(\lambda) + a_{\text{NAP}}(\lambda). \quad (1)$$

Here, $a_{\text{water}}(\lambda)$ is the absorption of water itself, $a_{\text{CDOM}}(\lambda)$ is the absorption of colored dissolved organic matter (CDOM), $a_{\text{ph}}(\lambda)$ is the absorption due to phytoplankton pigments, and $a_{\text{NAP}}(\lambda)$ is the absorption of non-algal particles. For most visible wavelengths (~400–700 nm), $a_{water}(\lambda)$ is small and accurately predicted from empirical data sets, including temperature and salinity effects (Röttgers et al., 2014).

The absorption of CDOM, which typically includes deteriorated organic material, is measured from water that has been filtered through a 0.22 μm filter. The spectrum of $a_{\text{CDOM}}(\lambda)$ in surface waters has normally an exponential shape with strong absorption within the visible spectrum and near-UV (>~350 nm). The absorption is the highest in the UV and negligible absorption in the near-infrared. Some regional relationships has been found between $a_{\text{CDOM}}(\lambda)$ and dissolved organic carbon concentration (Mannino et al., 2008), but no clear link has been found for the Nordic Seas (Makarewicz et al., 2018). More notably, the absorption spectral slope may be used to estimate the (bulk) origin of the dissolved organic matter, which is of particular relevance in the Arctic Ocean and the Fram Strait due to significant river run-off influence from Siberian rivers (Granskog et al., 2012).

Absorption by particulates, $a_p(\lambda)$, typically decomposed into the phytoplankton and non-algal particle absorption, $a_{\text{ph}}(\lambda)$ and $a_{\text{NAP}}(\lambda)$ respectively. While $a_{\text{NAP}}(\lambda)$ has a similar exponential shape as $a_{\text{CDOM}}(\lambda)$, but with a non-negligible near-infrared absorption, the phytoplankton absorption spectra $a_{\text{ph}}(\lambda)$ have distinct spectral features linked to different pigments (Mobley, 1994).

The light scattering coefficient $b(\lambda)$ has been less studied in terms of different constituents with direct measurements, often being decomposed into the pure water scattering $b_w(\lambda)$ and particulate scattering $b_p(\lambda)$, assuming negligible scattering from dissolved matter (Werdell et al., 2018). The former is well-described by theory, while $b_p(\lambda)$ is often estimated by the difference between non-water absorption $a_{nw}(\lambda)$ and beam attenuation measurements, defined as $c_p(\lambda) = a_{nw}(\lambda) + b_p(\lambda)$. The diffuse light attenuation coefficient $K_d(z)$ describing irradiance profiles should not be confused with $c_p(\lambda)$. The beam attenuation coefficient $c_p(\lambda)$ is mostly dominated by scattering and can be approximated as

$$c(\lambda) = c_0\left(\frac{\lambda}{\lambda_0}\right)^{-\gamma}, \quad (2)$$

where c_0 is the attenuation at a reference wavelength λ_0. The spectral slope γ is often linked to the particle size distribution of suspended particles (Boss et al., 2001; Slade and Boss, 2015; Organelli et al., 2020). The attenuation coefficient has also been extensively studied in relation to particulate matter in natural waters, acting as a proxy measurement for particulate organic carbon (POC) in the open ocean or suspended particulate matter in coastal waters (Behrenfeld and Boss, 2006; Hill et al., 2011; Neukermans et al., 2012; Boss et al., 2015; Rasse et al., 2017; Gardner et al., 2022).

Earlier optical studies in the Barents Sea

There is a large body of literature describing oceanographical and biological processes in the Barents Sea, given its important role as a productive shelf area and hot-spot for observed climate change manifestations. However, this has been largely limited to the open waters or marginal ice zone, and mostly in the summer season. Several studies of the optical oceanography have also been conducted, starting in the 1970s with pioneering measurements of irradiance profiles using early radiometric instrumentation (Aas and Berge, 1976). Similar observational investigations focused around the diffuse attenuation coefficient were also conducted in the early 1990s (Dallokken et al., 1994; Aas and Høkedal, 1996; Falk-Petersen et al., 2000). The greater Barents Sea region (including Svalbard) was summarized as being optically complex with large spatial and temporal variations.

More recent optical studies of the Barents Sea have used modern methodology that enables investigation of factors driving the underwater light availability. In connection with the International Polar Year in 2007–2008, optical measurements were collected on two research

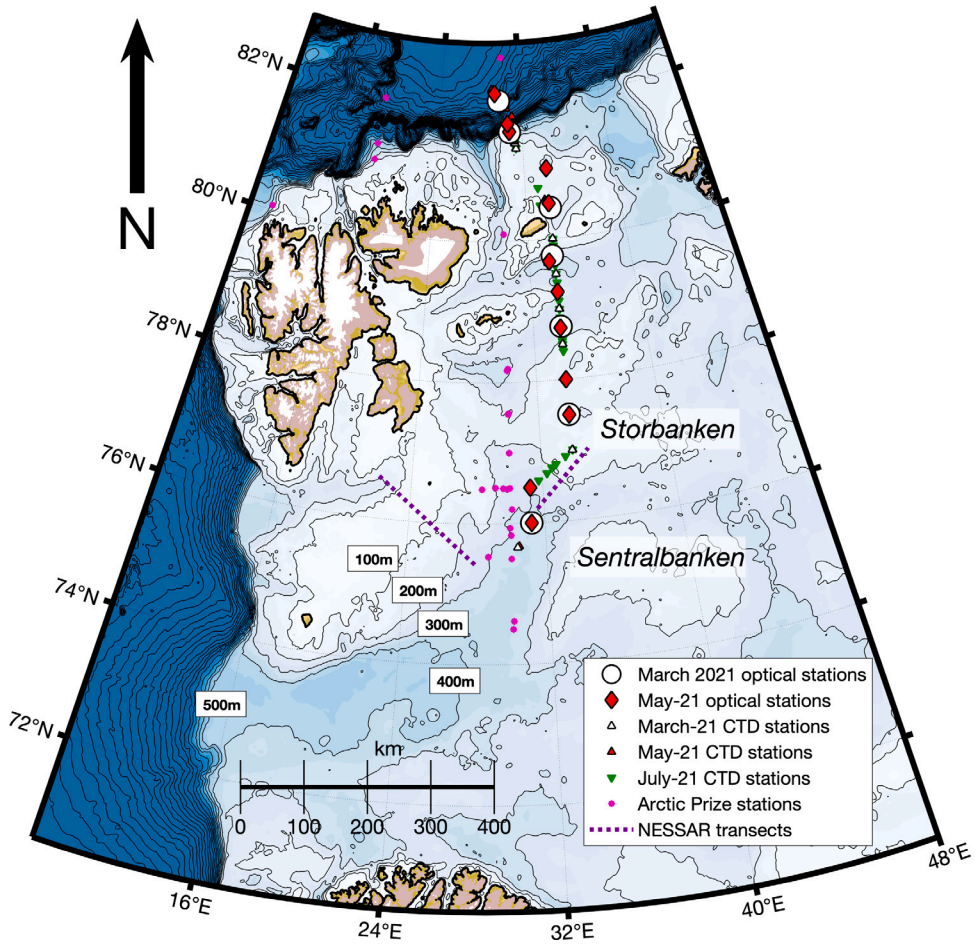

Fig. 1. Map of the Barents Sea, including locations of optical stations conducted in March 2021 (white circles), May 2021 (red diamonds), and additional CTD stations during these cruises (white and red triangles) and CTD stations during the July 2021 cruise (green triangles). Optical measurements from earlier field campaigns in the Barents Sea have also been included for comparison, namely *Arctic PRIZE* in 2018 (magenta circles) and *NESSAR* (purple dashed lines, rough estimate of transects).

cruises around the Polar Front in the central Barents Sea in August 2007 and May 2008. Both absorption measurements of particulate and dissolved matter was conducted along with radiometric measurements, leading to a series of publications (Hancke et al., 2014; Hovland et al., 2014; Erga et al., 2014). CDOM absorption was found to vary relatively little across the different hydrographic regimes, and blooms of strongly scattering *coccolithophore* were found to significantly affect both the underwater light regime and the spectral irradiance reflectance, leading to 20%–40% overestimation of primary productivity in satellite products. Through the Arctic PRIZE project, three cruises were conducted in 2018 collecting *in situ* optical measurements in roughly the same study area as this study, but only briefly entering ice-covered waters (Kostakis et al., 2020), as the sea ice extent was very low in 2018 (Bailey et al., 2021). This data set was used to develop bio-optical parameterizations linking glider measurements to absorption and scattering properties, which is used in a recently published bio-optical model to estimate the underwater light field in various locations in the greater Barents Sea area (Connan-McGinty et al., 2022). Lokhov et al. (2020) carried out simultaneous LISST-Deep and turbidity measurements in the Barents Sea in June 2019, demonstrating how backscattering and particle concentration relationships can be affected by particle composition. Another recent study in Storfjorden, east of Spitsbergen, describes the rather high optical complexity in the coastal waters adjacent to the Barents Sea, affected by land runoff, sea ice melt, subsurface phytoplankton blooms and bottom resuspension (Petit et al., 2022).

In addition to the *in situ* optical surveys, there have been numerous ocean color remote sensing studies of the regional primary productivity, again obviously limited to the open-water season or regions (e.g. Kogeler and Rey, 1999; Oziel et al., 2017; Silva et al., 2021). However, satellite products require strong assumptions about the optical properties and their vertical structure, are often not regionally validated, and are challenging to use in highly cloud- and ice-influenced waters like the Barents Sea (Castro de la Guardia et al., this issue).

Despite the aforementioned studies, there is rather little information on the seasonal evolution of optical conditions, and even more so seasonally or regionally from the currently heavily ice-covered northern parts of the Barents Sea. This study presents optical measurements collected during several seasonal south–north transects in the northwestern Barents Sea shelf. The seasonality of this region is being studied in detail through the Nansen Legacy project, and this study aims to describe the seasonal and spatial variability of optical properties across the seasonally ice-covered northern parts of the Barents Sea, to examine the factors driving the seasonality of absorption and scattering on a basin-scale. A companion paper submitted to this same special issue examines in closer detail the hydrographic changes following seasonal sea ice retreat and accompanying changes in nutrient and phytoplankton dynamics over the same seasonal transition (Koenig et al., this issue).

2. Material and methods

The main data collection was carried out during the *Nansen Legacy Q1* and *Q2* cruises onboard *R/V Kronprins Haakon* in March and May 2021, respectively (Gerland et al., 2022; Ludvigsen et al., 2022). The cruises repeated the same transect in the northern Barents Sea, following roughly the 33°E meridian, see Fig. 1. Measurements on the first

cruise started furthest south on March 5th, and the last station was conducted on March 17th on the north end of the transect. The work on the second cruise started on April 30th, and ended on May 14th, also going south-to-north. The *Nansen Legacy Joint Cruise 2-1* cruise in July 2021 onboard *R/V Kronprins Haakon* is also included in the study, but no dedicated inherent optical properties measurements were conducted on this cruise (Jones et al., 2022). This cruise also covered the same transect. Deployment of an optical profiling instrument package was conducted in March and May from the side of the ship, except on some on-ice stations where profiles were conducted through a hole in the ice. Water samples were primarily collected from the ship's CTD rosette, deployed through the moon-pool of the vessel, while surface water samples (less than 10 m) were collected from a Niskin bottle deployed over the side of the ship. Some surface samples were also collected from the ice stations. The sampling locations were chosen based on scientific interests from the research groups in the project and the many logistical constraints on a cruise in sea ice, yielding some variations in the exact locations and density of sampling locations.

In situ light absorption and attenuation measurements

The optical profiling package consisted of a SeaBird SBE37 SIP conductivity-temperature-depth (CTD) probe and a WET Labs ac-s spectrophotometer (Seabird Scientific). A WET Labs DH4 data logger was used to collect and merge the data from the different sensors. The ac-s measures the absorption and attenuation coefficient at 85 wavelengths (nominally ~80) between 400 and 750 nm, and is the most widely used *in situ* instrument for measuring absorption and scattering properties of the water column.

Profiling was done using a constant descent velocity (~0.3 m/s) down to a depth of 350 m (200 m for March cruise) or ~10 m above the ocean floor. Standard measurement protocols were followed, e.g. pre-flushing of the instrument at >10 m, subtraction of blank measurements, and temperature and salinity corrections (Moore et al., 1997). The attenuation coefficient was not fully corrected for the effects of temperature on instrument electronics (the corrections were developed for temperatures >0 °C, while the Barents Sea waters are often at sub-zero temperatures), and was consequently extrapolated to wavelengths larger than 688 nm using a second-order polynomial.

An extensively studied uncertainty in ac-s absorption measurements is the incomplete collection of scattered light by the reflective tube of the instrument (Röttgers et al., 2013; Kostakis et al., 2021). Even after correction, the associated uncertainty is estimated to be on the order of 25% in coastal waters, but less in clear oceanic waters due to a lower influence of non-algal particles from land. The measurement errors connected to instrument uncertainties, e.g. random fluctuations, drift and error propagation from blank measurements and calibration, have been estimated to be 0.01 m^{-1} for wavelengths <450 nm, and 0.005 m^{-1} for longer wavelengths, given that the instrument is optimally calibrated (IOCCG, 2018).

By comparing the measured ac-s data with the concurrent absorption coefficients measured from water samples, we chose the most suitable scattering correction (see Appendix for details). The proportional baseline method gave the best agreement for the absorption measurements in the May 2021 data set, and was applied to both cruises for consistency. Here, the corrected absorption measurements $a_{corr}(\lambda)$ are given by,

$$a_{corr}(\lambda) = a_{meas}(\lambda) - a_{meas}(\lambda_{ref})\left(\frac{c_{meas}(\lambda)/e_c - a_{meas}(\lambda)}{c_{meas}(\lambda_{ref})/e_c - a_{nw}(\lambda_{ref})}\right), \quad (3)$$

where $a_{meas}(\lambda_{ref})$ is the measured absorption at a reference wavelength in the near-infrared, where non-water absorption can be assumed to be negligible in oceanic waters. In our case, $\lambda_{ref} = 709$ nm. Furthermore, e_c is the estimated fraction of the true attenuation which is not detected by the ac-s due to the acceptance angle. This value was found to be 0.56 in the North Sea in Röttgers et al. (2013), but has been observed to vary considerably in other studies.

From the spectral ac-s measurements, several useful properties can be derived. An alternative observation of phytoplankton biomass is made by computing the absorption line height at 676 nm from *in situ* ac-s absorption spectra, $a_{LH}(676\ nm)$ using the following formula from (Roesler and Barnard, 2013),

$$a_{LH}(676\ nm) = a(676\ nm) - a(650\ nm) - \frac{676-650}{715-650} \times \left[a(715\ nm) - a(650\ nm)\right]. \quad (4)$$

The attenuation spectral slope γ is calculated from $c_p(\lambda)$ between 435 and 686 nm by curve-fitting Equation (2) using the Nelder–Mead method. The spectral slope can linked to the particle size distribution $N(D)$ in the water following

$$N(D) = N_0\left(\frac{D}{D_0}\right)^{-(\gamma+3)}, \quad (5)$$

where N_0 is the number concentration for particles with the reference diameter D_0 (Boss et al., 2001). Finally, the single scattering albedo σ is given by

$$\sigma = \frac{b(\lambda)}{c(\lambda)} = \frac{c_{ACS}(\lambda) - \left(a_{CDOM}(\lambda) + a_p(\lambda)\right)}{c_{ACS}(\lambda)}. \quad (6)$$

Here, $c_{ACS}(\lambda)$ is the concurrent attenuation measurements made with the ac-s and combined with water sample absorption measurements to calculate the scattering $b(\lambda)$.

Two optical sensors were deployed on the main Conductivity-Temperature-Depth (CTD) profiler of R/V Kronprins Haakon on all three cruises. The ship's CTD (Seabird SBE 911plus with double conductivity and temperature sensors) was deployed more frequently than the optical profiling package, and therefore has an unrivaled spatial coverage. Moreover, data sets from other research cruises without dedicated optical measurements increase the possible temporal coverage. The WET Labs C-Star transmissometer (SeaBird Scientific) yields the beam attenuation coefficient at 650 nm, c_{650}. Dissolved matter and pigment absorption influences to a small extent the attenuation at 650 nm, and c_{650} has therefore been found to a be a robust proxy measurement for particulate matter parameters like total suspended matter, chlorophyll biomass or particulate organic carbon, but generally requires development of regional empirical relationships (Behrenfeld and Boss, 2006; Neukermans et al., 2012; Rasse et al., 2017). Regular blank measurements are typically required for accurate attenuation measurements. Lacking this for the present data set, we utilize deep CTD casts to find a reference beam transmission T_r, which is the lowest beam transmission value recorded on each cruise (disregarding outliers). The attenuation coefficient is then given by

$$c_{nw}(z) = -\frac{\ln(T(z)/T_r)}{L}, \quad (7)$$

where $T(z)$ is the measured beam transmission at depth z and $L = 0.25$ m is the instrument path length. The reference values found for each cruise were respectively 93.688% (March), 93.179% (May), and 93.266% (July). Similar processing have been conducted in Neukermans et al. (2014) and Gardner et al. (2022), also in Arctic waters. The main uncertainty is the true attenuation coefficient at the reference depth (assumed to be zero), which is most likely on the order of 0.005 m^{-1} or less. Given the (relatively) low variations in temperature and salinity during each cruise, this correction method also negates the need for any temperature or salinity corrections at this wavelength.

Chlorophyll-a fluorescence was also measured on the main CTD on all cruises, using a factory-calibrated WET Labs ECO-FL chlorophyll fluorometer (Seabird Scientific, excitation wavelength 470 nm, emission wavelength 695 nm). While being a widely used sensor for measuring chlorophyll-a concentration, considerable uncertainties has been identified in the relationship between chlorophyll-a fluorescence and actual concentration (Roesler et al., 2017). The current recommendation is to multiply the measured values by two to achieve agreement with paired HPLC measurements for a global data set, but large

regional and species-specific variations are found. It is therefore necessary to validate *in situ* fluorometer measurements with laboratory measurements.

Temperature and salinity measurements from the ship CTD have also been used here to describe the hydrography of the transect, we refer to the companion paper for more details (Koenig et al.). All salinity measurements are reported on the Practical Salinity Scale (dimensionless).

2.1. Laboratory measurements

CDOM absorption measurements

Samples for colored dissolved organic matter (CDOM) were collected directly from the Niskin bottles by gravity filtration through a 0.22 µm cartridge filter and stored refrigerated in the dark in pre-combusted amber glass vials until measurement (cf. Petit et al., 2022). The spectral absorption coefficient of CDOM was measured using a liquid waveguide capillary cell (LWCC). Multiple absorption spectra were acquired using several repetitions (nominally 3) of sample and reference measurements (with purified water), each calculated as follows,

$$a_{\mathrm{CDOM}} = -\frac{1}{L}\ln\left(\frac{I_S(\lambda) - I_{DC}(\lambda)}{I_{\mathrm{ref}}(\lambda) - I_{DC}(\lambda)}\right). \tag{8}$$

Here, $I_S(\lambda)$ is the measured sample intensity, $I_{\mathrm{ref}}(\lambda)$ the reference intensity, and $I_{DC}(\lambda)$ the dark current intensity (all in digital counts). The instrument optical path length is $L = 1$ m. The measured spectra were corrected for temperature and salinity effects following Lefering et al. (2017), averaged to get a single spectrum for each sample, and smoothed to remove high-frequency oscillations due to an increased refractive index in the saline sample water.

The CDOM absorption spectrum can be estimated as

$$a_{\mathrm{CDOM}}(\lambda) = a_{\mathrm{ref}} \exp\left(-S(\lambda_{\mathrm{ref}} - \lambda)\right). \tag{9}$$

Here, λ_{ref} is a reference wavelength, typically 300 or 350 nm, while S is estimated slope using a wavelength range (e.g. 350–550 or 300–650 nm). The relationship between S and a_{ref} can give information on whether the dissolved organic matter has a pelagic or terrestrial origin (Granskog et al., 2012; Stedmon and Markager, 2001). In this study, the spectral measurement is curve-fitted to the exponential slope using the Nelder–Mead method (*fminsearch* in MATLAB). The CDOM absorption data is available from Sandven et al. (2023a,b).

Particulate absorption measurements

Water collected from the CTD rosette was filtered through Whatman GFF filters, nominally 1 liter filtered volume. Filtration was done rapidly after water collection and the filters were frozen in a -80 °C freezer.

Two independent quantitative filter techniques were used to measure the optical density of the filters. Both methods are based on placing filters inside integrating spheres. The "QFT-Perkin" method uses a Lambda 950 UV–Vis-NIR spectrophotometer (Perkin Elmer, USA) to determine the optical density (Röttgers and Gehnke, 2012), while the QFT-ICAM is a small portable integrating cavity absorption meter (Röttgers et al., 2016). QFT-ICAM has been found to give accurate absorption measurements in the visible and the near-infrared range, in particular due to its low scattering errors compared to other methods. The QFT-Perkin method gives superior results in the UV range, but is affected by residual scattering error. For both methods, the particulate absorption $a_p(\lambda)$ is computed using

$$a_p(\lambda) = \left(\mathrm{OD}_S(\lambda) - \mathrm{OD}_{\mathrm{ref}}(\lambda)\right)\frac{A}{V\beta}. \tag{10}$$

Here, $\mathrm{OD}_S(\lambda)$ is the measured optical density of the specific sample, corrected for any stray light or non-linearity effects, and $\mathrm{OD}_{\mathrm{ref}}(\lambda)$ is the corresponding reference optical density measured using a wet blank filter. Furthermore, A (m^2) is the filter patch area and V (m^3) is the volume of the filtered water. The path length amplification factor $1/\beta$ is technically defined as the ratio between the optical and geometrical path length in the measurement set-up, but operationally it describes all contributions of scattering to the measured signal in the absorption meter. The amplification factor has been extensively studied for different measurement set-ups throughout the years (Bricaud and Stramski, 1990; Stramski et al., 2015; Kostakis et al., 2021), and is considered the largest uncertainty factor for filter pad measurements with a typical sample-to-sample variation of around 15% for β (Röttgers and Gehnke, 2012; Röttgers et al., 2016; Lefering et al., 2016). To combine the two measurement, QFT-ICAM was used to find the near-infrared absorption coefficient, and an offset is subtracted from the QFT-Perkin absorption measurements to reach agreement between the two measured spectra at long wavelengths. The final values are consequently the QFT-Perkin measurements.

The filters were bleached using a 1% NaOCl solution for 1–3 min, after which the bleach is removed with a H_2O_2 solution, and measured ~12 h later using the QFT-ICAM set-up. The measured optical density yields the non-algal particle (NAP) absorption $a_{\mathrm{NAP}}(\lambda)$ using Eq. (10). The particulate absorption data is available from Sandven et al. (2023a,b).

Chlorophyll-a and phaeopigments

During the seasonal cruises, Vader (2022) determined the chlorophyll-a and phaeopigment concentrations throughout the water column. A known volume of seawater was filtered through Whatman GFF glassfiber filters (nominal pore size 0.7 µm). The filtered volume was nominally one liter, but lowered for samples with higher concentrations. Samples were measured onboard using a Turner 10-AU or Turner Trilogy fluorometer. For details see the Nansen Legacy Sampling protocol 2022.

Particulate organic carbon

Particulate organic carbon concentrations were measured using triplicate subsamples (500–1500 mL), which were filtered on pre-combusted Whatman GFF filters. Filters were stored at −20 °C, and analyzed on a Leeman Lab CHN Analyzer within one year, following procedures described in Reigstad et al. (2008) and the Nansen Legacy Sampling protocol 2022. POC values smaller than three times the blank values were excluded from the data set used in this study. Data is available from Marquardt et al. (2022a,b,c).

Sea ice concentration

The sea ice concentration is estimated from the satellite-borne AMSR2 passive microwave sensor, accessed through the University of Bremen daily sea ice concentration products (https://seaice.uni-bremen.de/sea-ice-concentration/amsre-amsr2/information/, last accessed on June 2nd, 2023). The data set, covering each day for every Nansen Legacy standard station (spatial gridded resolution 6.25 km). For each cruise, the average sea ice concentration for the entire cruise period was calculated for the different standard stations.

3. Results and discussion

3.1. Seasonality of optical properties

In Figs. 2–4, transects of the water column properties in the Barents Sea are shown, covering a distance of approximately 800 km from ~76°N to 82°N. The plots showing temperature, salinity, chl-a fluorescence and c_{650} are based on measurements from the main ship-CTD, and therefore has a much higher spatial resolution than the bottom four panels in Figs. 2 and 3, which were only done on selected stations. The graphical software Ocean Data View was used to produce the plots, using a weighed-average gridding to graphically interpolate the measurements in space between each depth profile. For

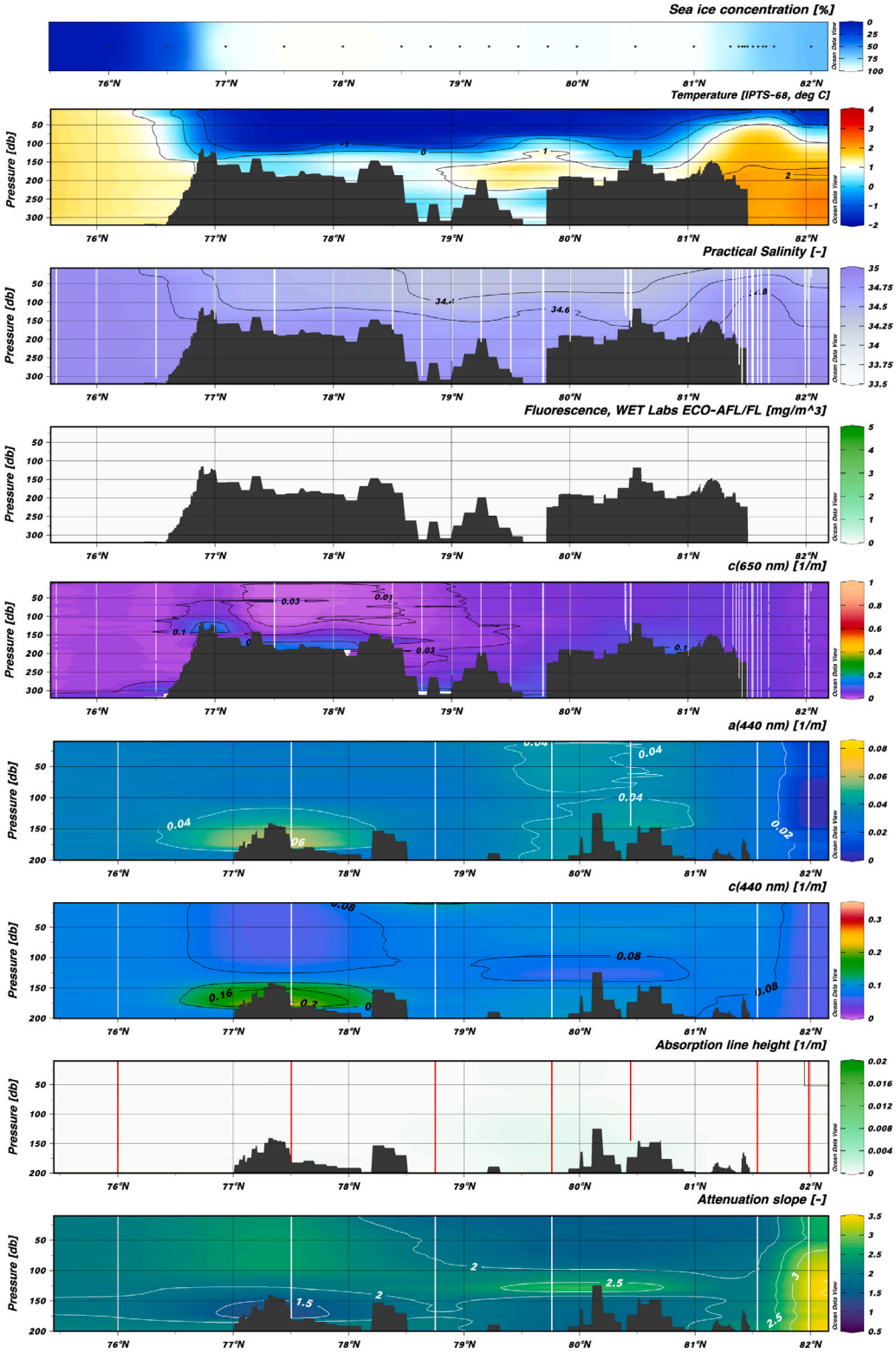

Fig. 2. Optical and hydrographic transects during the March 2021 cruise. Note the difference in depth range and horizontal frequency of stations between the first four (ship-based profiles) and last four (optical package) panels.

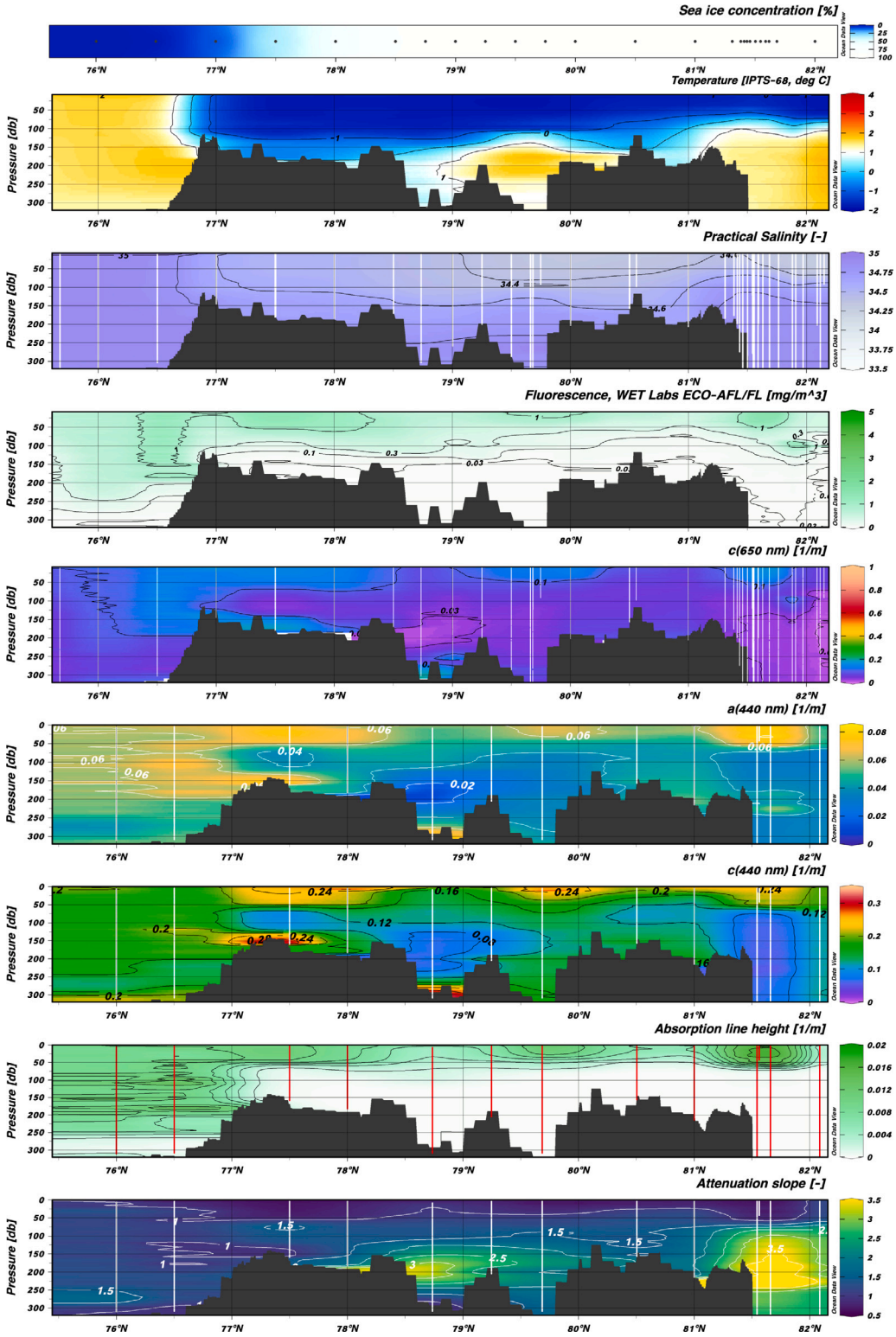

Fig. 3. Optical and hydrographic transects during the May 2021 cruise.

more detailed analysis on the hydrography, see Koenig et al., who examine the phytoplankton distribution in the context of sea ice, water masses, and light availability.

In March 2021, the absorption and attenuation (at 440 nm) were low and relatively uniform throughout the entire transect. A notable exception is a distinct increase in both a(440 nm), c(440 nm) and c_{650} near the ocean floor. This is due to resuspended seafloor sediments caused by turbulent interactions in the ocean bottom boundary layer (Trowbridge and Lentz, 2018). Throughout the seasonal transect, the enhanced attenuation could be seen more than 50 m above the seafloor. Similar features were also observed in the adjacent Storfjorden (Petit et al., 2022). Resuspended sediments have a well-documented effect on optical properties, in particular for particle sizes on the order of 0.5–50 μm (Hill et al., 2011; Slade and Boss, 2015). Note that the graphical interpolation used will occasionally exaggerate the horizontal extent of these features.

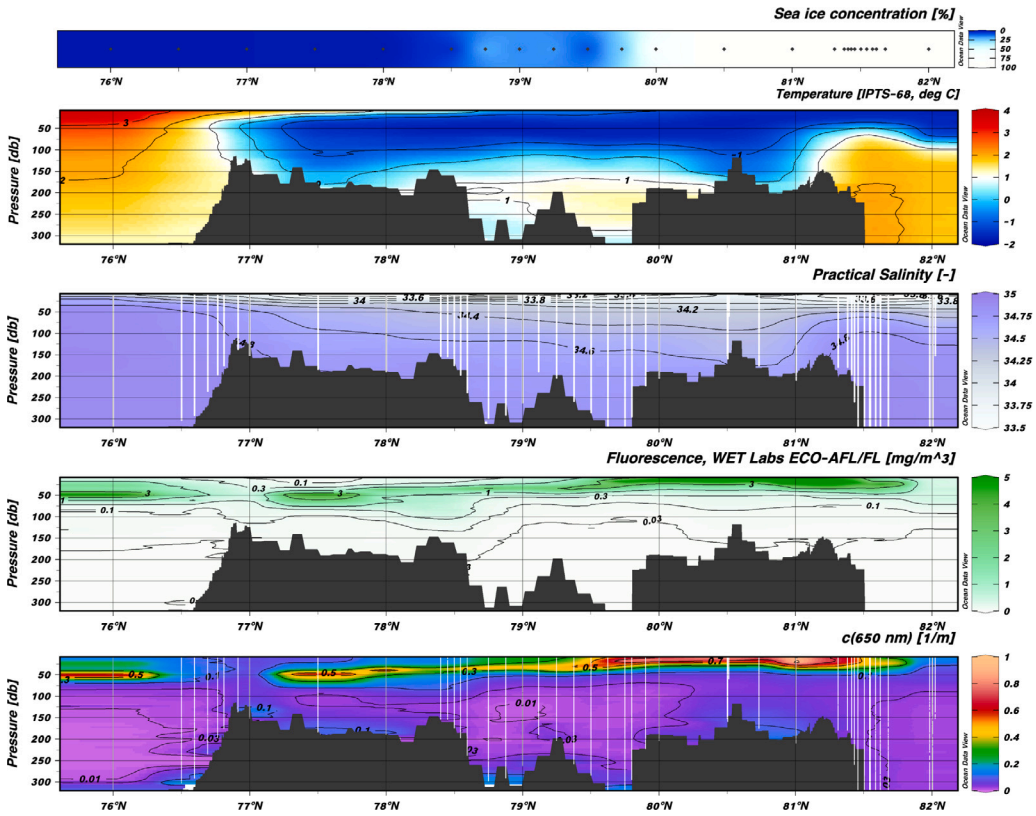

Fig. 4. Optical and hydrographic transects during the July 2021 cruise.

The low and uniform values of $a(\lambda)$ and $c(\lambda)$ in the rest of the water column agrees well with chlorophyll fluorescence measurements (both *in situ* and benchtop measurements), which indicates very low phytoplankton biomass (see also Koenig et al.). The measured $a_{LH}(676\ nm)$ supports the description of a Barents Sea in "winter hibernation" in terms of primary production, with pigment absorption and chlorophyll fluorescence at or below the detection limit.

While the temperature and salinity gradients show relatively subtle variations from March to May, the optical and biological properties have changed over the two months due to increased light availability, see Fig. 3. Estimates from PAR depth profiles, presented in Koenig et al., showed that the euphotic depth increased from zero to ~30 m in May. The increased primary productivity, as observed from the chl-a fluorescence and $a_{LH}(676\ nm)$, led to higher absorption and scattering coefficients. Stronger spatial variability is also observed. At the very northern end of the transect, north of the continental slope to the Nansen Basin, an under-ice phytoplankton bloom is observed, with chl-a concentrations higher than 1 g/m^3 occurring down to 55 m (estimated from *in situ* chl-a fluorescence). Although at sampling the relevant area was reportedly covered by approximately 1 m thick sea ice with ~90% areal concentration (Ludvigsen et al., 2022), there was still enough available light to support photosynthesis in the water column. Intermittent leads in even thicker sea ice have been observed to enable under-ice blooms (Assmy et al., 2017). On the northern margin of the Barents Sea, there is an increased influence from warm Atlantic water along the continental slope passing through the Fram Strait and north of Svalbard, often referred to as Whaler's Bay (Graham et al., 2019; Lundesgaard et al., 2022). Consequently, the sea ice cover may be more variable and on average lower than further south (also during winter), and the vertical stratification can be stronger. Here, the lower boundary of the bloom coincides with the pycnocline of the surface mixed layer. Small-scale variability in the thermocline and chl-a fluorescence at ~ 81.9°N suggests some lateral mixing of phytoplankton, but the graphical interpolation may exaggerate the features.

Further south, in the interior northern Barents Sea, the under-ice phytoplankton productivity was lower and more patchy as observed from both $a_{LH}(676\ nm)$ and chl-a fluorescence. This coincided with near 100% sea ice concentration, but a highly varying ice thickness from 0.1 to 1.5 m (Ludvigsen et al., 2022). The measured attenuation coefficient remains relatively high throughout most of the ice-covered transect, which indicates deteriorating organic matter after a bloom. In Section 3.3, we show that attenuation at 650 nm provides robust estimates for POC concentration in these waters. Nutrient measurements, presented in the companion study (Koenig et al.), shows a slight decrease from March to May, indicating that the phytoplankton production has been ongoing for some time, but not yet been depleted at any depth.

A noteworthy feature is seen at the southern end of the transect, south of the ice edge. Not only chl-a fluorescence, but also $a_{LH}(676\ nm)$, absorption and attenuation coefficients show elevated values indicating phytoplankton biomass extending down to 200 m at two stations. This is close to the euphotic depths observed in even the clearest oceanic waters (Kaartvedt et al., 2019). The well-mixed hydrography, and a reported storm short time before the stations were sampled (Ludvigsen et al., 2022), suggests that surface water masses containing phytoplankton have been potentially transported downwards by wind-driven mixing. The vertical mixing may have been further modified by the nearby Polar Front, the horizontal thermocline between cold Arctic and warm Atlantic water. However, the hydrographic measurements lack sufficient resolution to determine the distance to the front.

For the July cruise (Fig. 4), no absorption and spectral attenuation properties were measured. However, the highly resolved fluorometer and beam attenuation (c_{650}) measurements give a valuable view into the late summer conditions along the same transect. The ice edge had receded further north and ice concentrations in the interior northern Barents Sea were much lower than in May. Here, the classically described marginal ice-zone bloom dynamics can be clearly

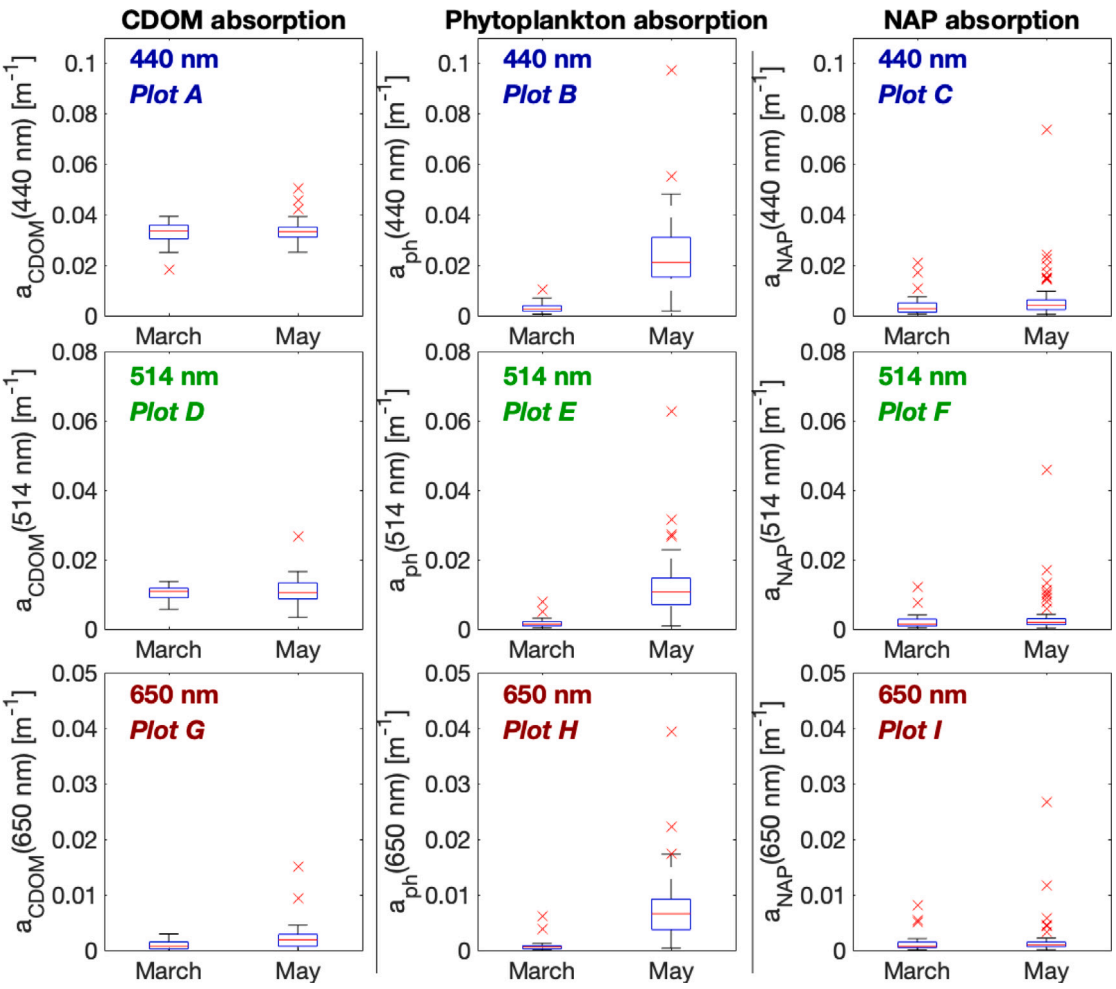

Fig. 5. Box plots showing the seasonal differences between two cruises in March and May 2021 of CDOM, phytoplankton and non-algal particle absorption, measured from water samples. Plots A, D and G shows the CDOM absorption coefficients at 440, 514 and 650 nm respectively. Fig. 5B, E and H shows the corresponding absorption properties for phytoplankton pigments, and Fig. 5C, F and I shows non-pigmented particle absorption. The box plots display the median values, quartiles (box edges), the non-outlier range (1.5 times the interquartile range) as whiskers, and any outlier values as crosses. Note the *y*-axis changing with wavelength, but constant for all constituents.

seen from both c_{650} and chl-a fluorescence transects. In the north, a strong under-ice surface bloom is present. Further south, the surface bloom has transformed into an subsurface chlorophyll maximum, due to nutrient depletion in the surface mixed layer (Koenig et al.). The estimated compensation depth isolumes in the same study also roughly follows the subsurface chlorophyll maximum, suggesting an interplay between light- and nutrient-limitation here. The transition happens around 79.5–80°N, which was also the approximate location of the sea ice edge at the time of the cruise (Fig. 4).

The lowermost panels in Figs. 2 and 3 show the attenuation spectral slope γ. During the March 2021 cruise, the estimated attenuation slopes indicated a comparatively high concentration of small particles throughout the water column, except for the bottom boundary layer where larger particles contribute more. In the May 2021 measurements, we see a stronger contrast between the phytoplankton-influenced waters, with low γ-values (more large particles) and the deeper clear waters with very high γ-values (predominantly small particles). CDOM absorption can also play a part when the particle concentration is very low, giving abnormally high γ-values.

3.1.1. Water constituents

In Fig. 5, we take a closer look at the seasonal differences in absorption properties of the water constituents, with spatial variability is shown through box plots. The absorption at 440 nm for CDOM, phytoplankton and NAP is plotted in Fig. 5A, B and C. During the March 2021 cruise, the phytoplankton and NAP absorption is uniformly low, while CDOM absorption in higher, but still spatially uniform throughout the transect. Further, looking at absorption at 514 nm (Fig. 5D, E, F), we see that CDOM dominates absorption even in the green part of the spectrum, while in the red part (650 nm, Fig. 5G, H and I) the absorption of all non-water constituents is very low during the March 2021 cruise. We see a dramatic increase in absorption from March to May for phytoplankton and non-algal particles, while CDOM absorption remains nearly constant, but with a slightly higher variability.

We compare CDOM and particulate absorption (surface waters shallower than 50 m) with other Barents Sea data sets in Figs. 6 and 7. This paints a different picture of the CDOM absorption in particular. While $a_{CDOM}(440\ nm)$ is nearly constant from January to May, even during spring blooms, it increases during the summer months. This is similar to dissolved organic carbon, which also shows greater variability in the later part of the year compared to the spring (Maria Digernes, personal communication, 2022).

The particulate absorption measurements collected during the Arctic Prize expeditions in 2018 also show considerable seasonal variability (Kostakis et al., 2020). In 2018, the ice extent was particularly low in the Barents Sea (Bailey et al., 2021). They observed a stratified surface layer containing a strong bloom in April–May, which explains the higher particulate absorption values than in May 2021. The April–May 2018 transect was also located further south, not extending north of the Polar Front.

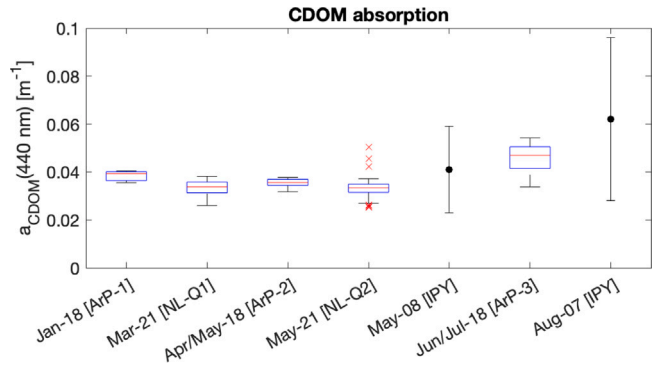

Fig. 6. The variability of CDOM absorption in Barents Sea surface waters (upper 50 m) at 440 nm as a function of time of the year, including additional data sets from the study area. The Arctic Prize (ArP) project collected optical measurements in January, April–May and June–July 2018 (Kostakis et al., 2020). The box plots display the median values, quartiles (box edges), the non-outlier range (1.5 times the interquartile range) as whiskers, and any outlier values as crosses. During the International Polar Year (IPY) in 2008, CDOM measurements were also conducted in the Barents Sea around the polar front in May and August. Here, only the mean absorption coefficient and standard deviation are shown due to data availability.

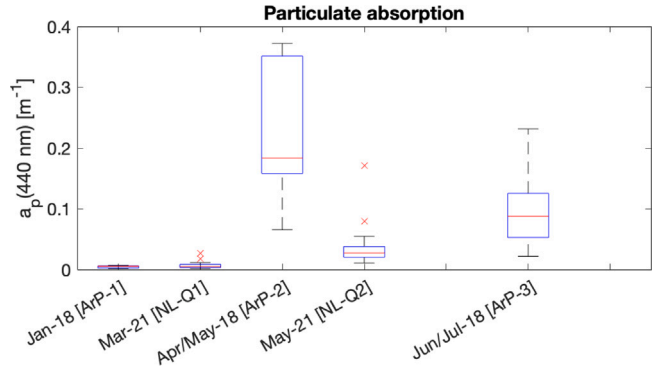

Fig. 7. The variability of particulate absorption in Barents Sea surface waters (upper 50 m) at 440 nm as a function of time of the year, similar to Fig. 5. The figure includes additional measurements from the Arctic Prize (ArP) project, collected in January, April–May and June–July 2018 (Kostakis et al., 2020).

3.2. Drivers of Barents Sea optical properties

The seasonality and spatial variations in the optical properties are typically driven by variations in ocean constituents. These variations can also be observed with other bio-geochemical properties, such as chlorophyll pigment concentration and dissolved and particulate organic carbon. Water masses influenced by terrestrial run-off have a lower salinity than oceanic water masses, and can have altered optical properties due to sediments or humic (organic) material. A detailed water sample analysis can give us a good assessment into what drives the variability of absorption. The scattering or attenuation properties are more challenging to assess, since they are measured *in situ* without any fractionation.

3.2.1. CDOM

The spectral absorption coefficient has been frequently associated with meteoric water, especially in the Arctic Ocean and the Fram Strait, which receives a disproportionately large amount of the global terrestrial run-off, particularly from Siberian rivers (Granskog et al., 2012; Goncalves-Araujo et al., 2018). The relatively low biological activity and inhibited ultraviolet-bleaching under sea ice causes the dissolved organic to degrade slowly. The optical variability in the central Arctic Ocean have in fact been observed to be mainly driven by CDOM concentration. In this data set, $a_{CDOM}(\lambda)$ was found to have little variation both seasonally and spatially. In Fig. 8, the mean $a_{CDOM}(\lambda)$ of all samples are plotted together with 10% and 90% percentiles (shaded areas). The relative standard deviation at 350 nm is only 13%, and a similar variation can be seen for the spectral slope. In Fig. 9, $a_{CDOM}(350\ nm)$ is plotted as a function of salinity, which has in other studies been observed to have a negative linear relationship with $a_{CDOM}(\lambda)$ due to river run-off (Kostakis et al., 2020). However, we see no evidence of trends for either salinity or temperature in this data set for either $a_{CDOM}(350\ nm)$ or the spectral slopes. In fact, a recent study in adjacent Storfjorden, east of Spitsbergen (Petit et al., 2022), shows that even in near-coastal waters there can be a *positive* relationship between salinity and $a_{CDOM}(\lambda)$, because CDOM concentrations are diluted by melting sea ice that creates a fresh surface layer (cf. Granskog et al., 2015). Consequently, any relationship between CDOM and salinity are connected with large inherent uncertainties in polar (surface) waters.

The two exponential models fits well with the data in two different ranges. In the UV part of the spectrum, the model $a_{300}\exp(S_{300-600}(\lambda - 300))$ provides good agreement, while the model $a_{350}\exp(S_{350-550}(\lambda - 350))$ fits best for all wavelengths larger than 350 nm, including the visible spectrum.

The average absorption spectrum of non-algal particles is also shown in a similar manner in Fig. 8. These spectral absorption coefficients are considerably lower than for $a_{CDOM}(\lambda)$ for wavelengths smaller than ~500 nm. The spectral slope is lower, but the variability is significantly greater. Some variability can be attributed to a lower signal-to-noise ratio in the filter measurements, but $a_{NAP}(\lambda)$ is also connected to a greater natural variability due to sediment resuspension or decaying phytoplankton.

3.2.2. Particulate absorption

In Fig. 10, two relevant spectral ratios for the discussion that follows are plotted for the both cruises. Fig. 10A shows the relative contribution of phytoplankton absorption to the total particulate absorption, $a_{ph}(\lambda)/a_{part}(\lambda)$. The May 2021 measurements show a strong spectral variability, in particular at long wavelengths where the 676 nm absorption peak is distinct, along with the increasing domination of $a_{NAP}(\lambda)$ above 700 nm. Within the visible range, the phytoplankton absorption mostly contributes 70% or more. By contrast, we see in the March 2021 measurements an almost equal contribution from pigmented and non-pigmented particulate matter (~30%–60%), with a low spectral variability. The measured absorption coefficients were also very low for the March 2021 cruise, meaning that noise can have a large impact on the perceived variability. Consequently, most of the natural variability in the particulate absorption within the visual spectrum is driven by pigmented particles, i.e. phytoplankton. In Fig. 10B, the single scattering albedo σ is shown. We see an overall domination by scattering processes for the May 2021 cruise, mostly higher than 80% with the exception of shorter wavelengths, which is typically for the open ocean. For the March 2021 cruise, absorption have a larger contribution to the attenuation, but as for Fig. 10A the absolute values were low during March 2021, and large relative measurement uncertainties could drive most of the variability.

Several studies have linked variations in particulate and non-water absorption to chlorophyll-a or POC concentration, often using a power-law relationship on the form

$$a(\lambda) = A(\lambda)c^{B(\lambda)}, \tag{11}$$

where c is the chl-a or POC concentration, and A and B are curve-fitted coefficients (Bricaud et al., 1998; Rasse et al., 2017; Pavlov et al., 2017). We conduct a similar analysis here. In Fig. 11A, a distinct trend between chl-a and $a_p(440\ nm)$ is visible. However, a power-law relationship derived from measurements in the global ocean (Bricaud et al., 1998), shown as a dashed line, does not show a high level of agreement with the observational data set. Another power-law relationship (dashed-dotted line) derived from observations of an under-ice *Phaeocystis pouchetii* bloom north of Svalbard in 2015 shows a better

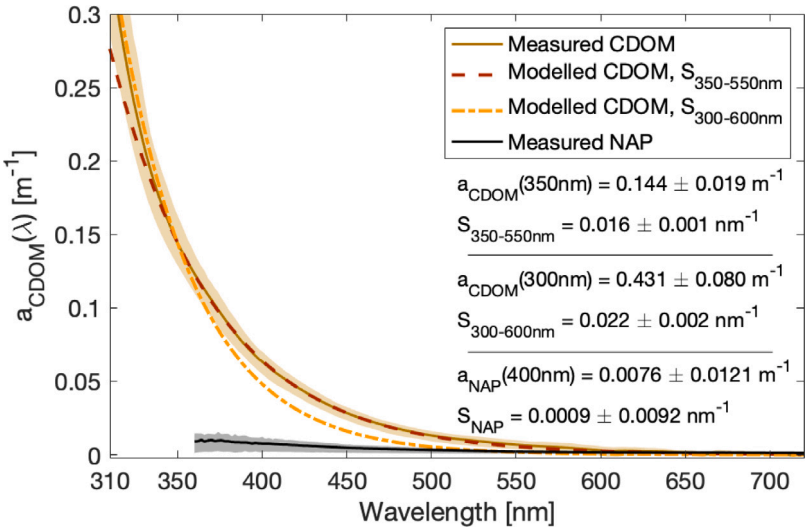

Fig. 8. Mean CDOM absorption spectrum (solid brown line) plotted together with the 10 and 90% percentile of the measurements (shaded area). The black solid line shows a corresponding spectrum for non-algal particulate absorption. The dashed (red) and dashed-dotted (orange) lines shows parametrizations of $a_{CDOM}(\lambda)$ using measurements in the range 350–550 and 300–600 nm, respectively.

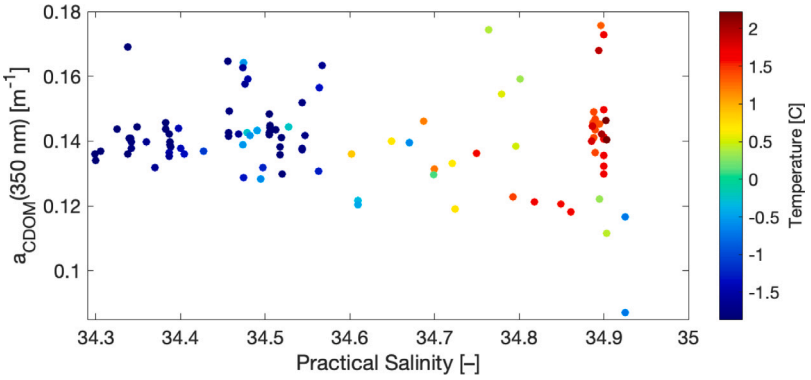

Fig. 9. CDOM absorption at 350 nm plotted as a function of salinity and temperature (color on markers).

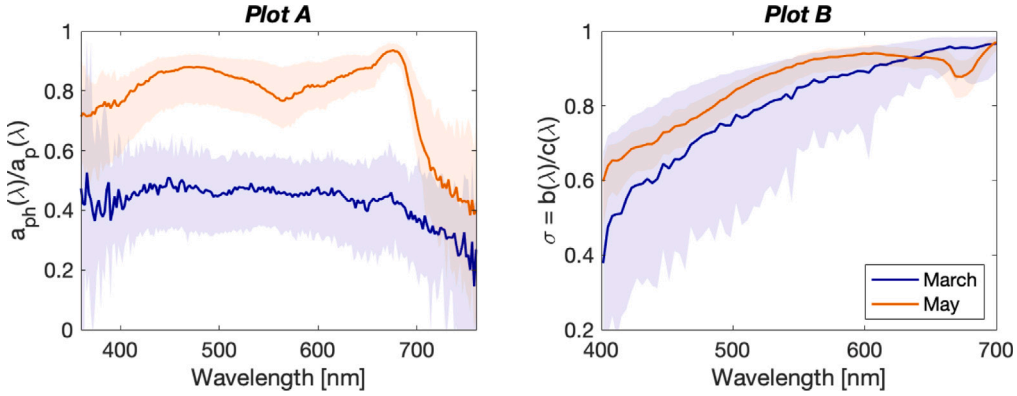

Fig. 10. Fig. 10A shows the relative contribution of pigmented particles to the particulate absorption as a function of wavelength, with the median plotted as a solid line, and the 10% and 90% plotted as shaded areas. The relative contribution of scattering to attenuation, the single scattering albedo σ, is corresponding displayed in Fig. 10B. Here, the absorption coefficient is calculated from combining water sample measurements and the attenuation is from concurrent ac-s measurements.

agreement with our measurements (Pavlov et al., 2017). This suggests that the under-ice absorption and chl-a relationship may be specific for this environment. A likely cause is that under-ice phytoplankton is adapted to a strongly light-limited environment (Pavlov et al., 2017).

A similar relationship could also be found between POC and particulate absorption, see Fig. 11D, E and F. The goodness-of-fit of this relationship varied less with wavelength than the chl-a relationship, which was more strongly linked to the pigment-specific wavelengths.

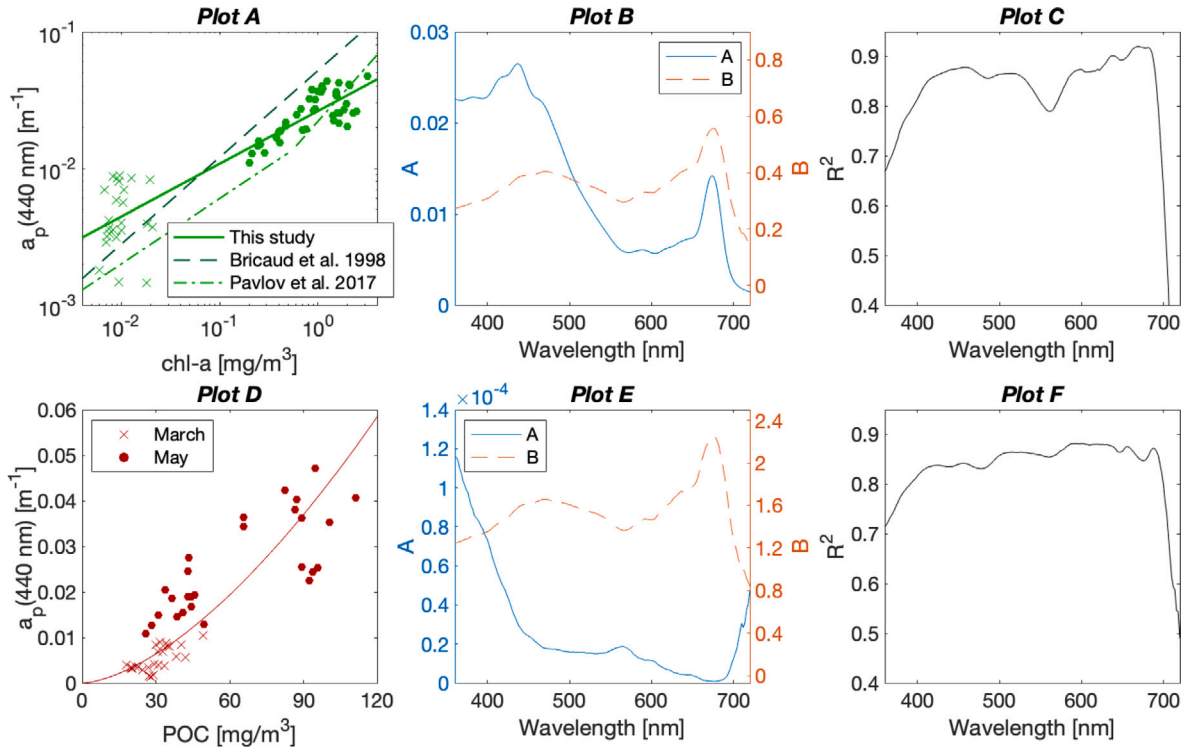

Fig. 11. The relationship between POC and chl-a concentrations and the particulate absorption coefficients measured from water samples. The scatter plots in Fig. 11A and D illustrates the trends at 440 nm, and Fig. 11B and E display the power law coefficients $A(\lambda)$ and $B(\lambda)$. In Fig. 11C and F, the spectrally resolved coefficients of determination R^2 are shown.

POC may therefore act as an alternate predictor of particulate absorption to chl-a. A larger and more varied data set may help us determine whether this relationship is more robust to photoacclimatization or other relevant factors in ice-influenced marine waters.

3.2.3. Scattering

Fig. 12 shows similar comparisons between the measured scattering coefficients and chl-a and POC concentrations. Scattering coefficients are calculated from ac-s attenuation and corresponding water absorption measurements, similar to Eq. (6). The goodness-of-fit is visibly lower in both the scatter plots and the calculated R^2-values compared to particulate absorption relationships. One reason could be more propagated errors from calculating the scattering (the ac-s measurements were often close to the sensitivity limit), and also from the fact that when combining *in situ* and water sample measurements, there might be some differences in sampled water mass, in particular for strong vertical gradients. The POC-b relationship is generally more robust than the chl-a relationship, especially considering the smaller range of POC-values measured compared to chl-a. There are also fewer extreme outliers.

In literature, attenuation or scattering coefficients are often linked to particulate matter quantities such as SPM or POC, typically particles smaller than 50 µm. In particular attenuation has been related to POC and phytoplankton biomass in several studies (Rasse et al., 2017; Huot et al., 2007). There is a also strong dependency of the particle size distribution on the scattering properties. Comparing the attenuation spectral slope γ with the attenuation coefficient at 650 nm (less influenced by absorption), see Fig. 13A, we see that a high attenuation coefficient is associated with a flatter spectral shape (no spectral variation for $\gamma = 0$). Consequently, a presence of larger particles (typically on the order of 10–50 µm) can be associated with the increased attenuation. A similar analysis is conducted for the spectral scattering coefficient in Fig. 13B. An exponential relationship is found between the spectral slope γ_b and the scattering coefficient at 650 nm, b_{650}. Assuming that we know b_{650}, for instance estimated from POC or C-Star measurements, we can approximate the spectral scattering as

$$b_p(\lambda) = b_{650}\left(\frac{\lambda}{650}\right)^{-2\times\exp(-17.358\times b_{650})}. \quad (12)$$

3.3. Evaluation of optical proxies for chl-a and POC

In this section, we evaluate how well bio-optical sensors estimate POC and chl-a concentrations. Even though these sample measurements have been routinely done, such sensor-based estimates can greatly enhance the spatial and temporal resolution of POC and chl-a observations. Scatter plots comparing beam attenuation coefficients measured with the C-Star transmissometer (c_{650}), *in situ* chl-a fluorometer (ECO-FL) and POC and chl-a concentrations measured from water samples are shown in Fig. 14, and Table 1. Measurements from the March (late winter), May (spring) and July (summer) cruises have been used. *In situ* chl-a fluorometers have been found to have regional biases throughout the global ocean, and must be regionally validated (Roesler et al., 2017). In Fig. 14A, we see good agreement across several orders of magnitude between the *in situ* chl-a fluorescence and the chl-a concentration from water samples. By introducing a simple linear correction for the *in situ* measurements,

$$[\text{chl}]_{\text{corr}} = A \cdot [\text{chl}]_{\text{meas}} + B, \quad (13)$$

the mean relative error is reduced from 112% to 51%. Some of the remaining uncertainty may be attributed to the sensitivity limit of the fluorometer, but also to the distinct seasonal differences between May and July 2021 at the higher chl-a concentrations. The seasonal variability can be explained by many different factors like variability in the phytoplankton species, growth phase, nutrient limitation, grazing, photoacclimation and non-photochemical quenching. Identifying the key drivers of the fluorescence variability in this specific region require a more extensive data set. By comparison to Fig. 14A, relationship

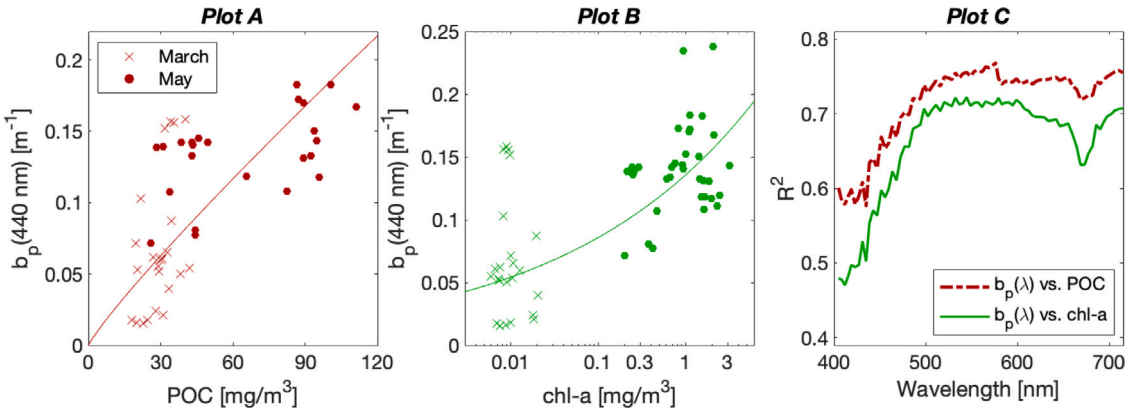

Fig. 12. The POC and chl-a relationships with non-water scattering coefficients, measured with concurrent ac-s and water sample measurements. The scatter plots in Fig. 12A and B illustrates the relationships at 440 nm, while Fig. 12C show the spectrally resolved coefficients of determination R^2 for both relationships.

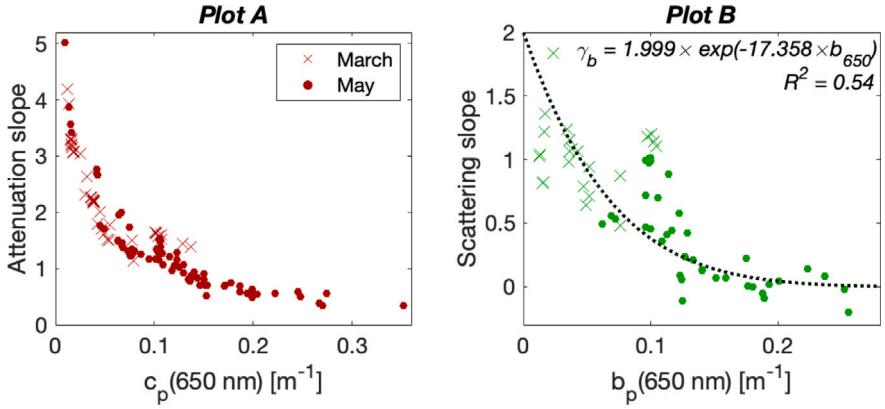

Fig. 13. The relationship between attenuation coefficient at 650 nm and the attenuation spectral slope γ is shown in Fig. 13A. An equivalent relationship is shown in Fig. 13B between scattering coefficient at 650 nm and the scattering spectral slope γ_b.

between c_{650} and chl-a is significantly worse as seen in Fig. 14B. Especially when considering low-productivity water masses, such as in March 2021, there is very low agreement between the measurements.

Fig. 14D shows the POC-c_{650} relationship, with the linear curve-fit plotted as a black dashed line (curved due to the log-transformed axis) and a power-law relationship plotted as a green solid line. The linear model fits the measurements better throughout most of the data range, but the power-law model is more realistic in the low end. At low values, both POC and c_{650} may both have large relative errors. There also seems to be low degree of seasonal bias in this relationship. The relationship between ECO-FL measurements and POC, shown in Fig. 14C, is influenced by several large outliers, some seasonal differences between May and July 2021, and an overestimation of POC at the low end due to the sensitivity limit of the fluorometer.

Overall, this analysis demonstrates a reasonable agreement between chl-a concentration and ECO-FL measurements, as well as POC and the attenuation coefficient. This is supported by statistical parameters shown in Table 1. Uncorrected ECO-FL data has a large relative error in comparison with corresponding chl-a water samples, which is greatly improved by applying a linear correction to the *in situ* measurements. The uncertainty is further reduced by treating the May and July data sets separately (March measurements are treated with the "May relationship", but are nevertheless clustered around zero). In Table 1, the two approaches are denoted "all data" and "seasonal split". The increase in MRE for the seasonal model is likely due to larger residuals for very low values.

It is challenging to compare POC and chl-a relationships due to differences in magnitude and range. The MRE is smaller for the POC-estimates, but MRE can be biased towards very small values that are plentiful in the chl-a data set. Meanwhile, NRMSD is more biased towards large values, so that POC-estimates are comparatively worse based on this parameter. Based on the statistical parameters calculated here, the in situ fluorescence seems to be a better proxy for POC than c_{650}. This could be explained by inorganic material contributing to the c_{650} in the bottom boundary layer, where the POC content is low and ECO-FL measurements are at the noise limit. Increases in POC and chl-a concentrations were also correlated during these cruises, while later in the year there may be a clearer decoupling. Nevertheless, Fig. 14B and D support that c_{650} provides additional information to the chl-a concentration, which is correlated to the POC concentration.

4. Conclusion

In this study, the optical properties of the seasonally ice-covered northwestern Barents Sea water masses have been investigated from two perspectives, seasonal and spatial variability and physical drivers. Comparing comprehensive field measurements made in March and May 2021 along a ~800 km south–north transect across the polar front, we see a large temporal difference in absorption and attenuation properties, going from a ocean system in a hibernation-like state (negligible phytoplankton biomass) to a more recognizable system from the Arctic Ocean with surface blooms developing under a largely ice-covered sea surface (cf. Koenig et al.). Surprisingly, the phytoplankton accumulation started while the mixed layer was still very deep compared to the compensation irradiance depth. As reported in earlier studies in the Barents Sea, CDOM absorption is low and varies relatively little throughout the spring months, but other studies indicates that it increases in the summer months. The Polar Waters in northern Barents

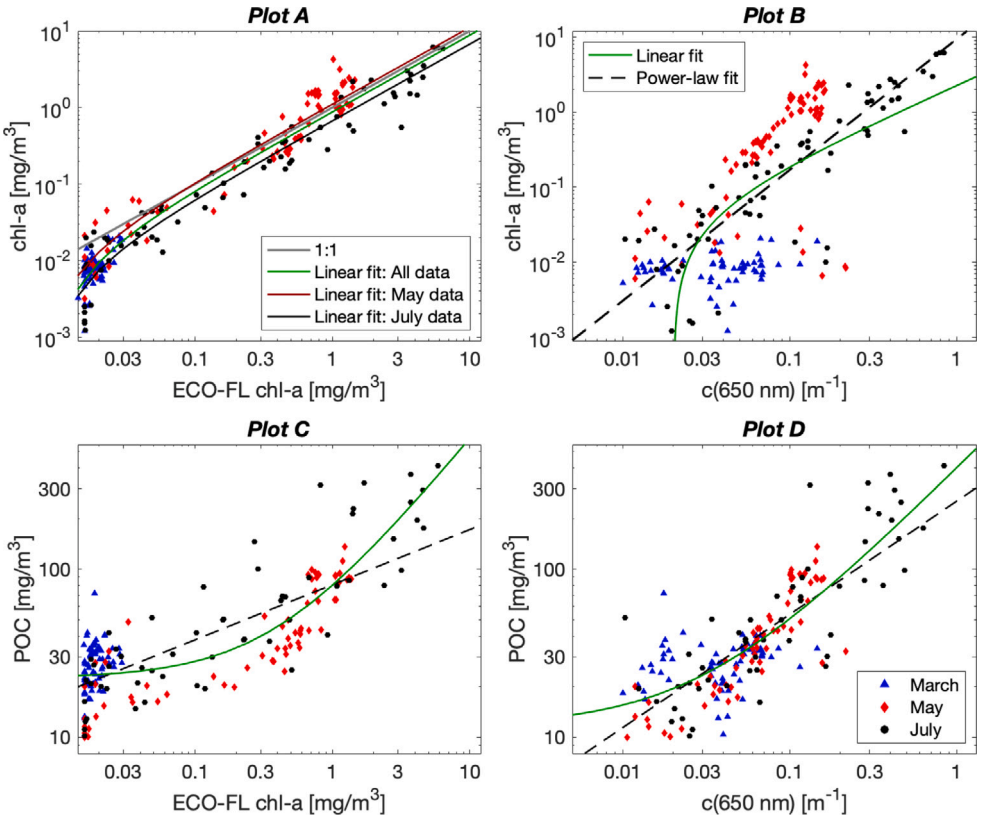

Fig. 14. Comparative plots for the *in situ* fluorescence of chl-a (ECO-FL) and beam attenuation (c_{650}) measurements, with chl-a and POC concentration from water samples.

Table 1
Statistical relationships for the quantities compared in Fig. 14. All regressions have been made on log-transformed data (cost function CF = $\Sigma(\log_{10}(y_{mod}) - \log_{10}(y_{obs}))^2$) using the Nelder–Mead method. Model-assessment variables are calculated with non-transformed data (y_{mod} vs. y_{obs}); RMSD is the root-mean-square deviation, NRMSD is the normalized RMSD (divided by $\max(y_{obs}) - \min(y_{obs})$), MAD is the median absolute deviation, and MRE is the mean relative error. Number of samples are given by n.

Relationship	Model	A	B	n	R^2	RMSD [mg/m^3]	NRMSD [%]	MAD [mg/m^3]	MRE [%]
ECO-FL vs. chl-a	1:1	–	–	194	0.70	0.55	8.85	0.016	117.30
(all data)	$Ax + B$	0.883	−0.008	194	0.73	0.52	8.40	0.011	49.44
(seasonal split)	$Ax + B$	–	–	194	0.78	0.47	7.63	0.016	54.17
(May)	$Ax + B$	1.1137	−0.009	76	0.55	0.57	13.33	0.222	48.77
(July)	$Ax + B$	0.6752	−0.006	71	0.82	0.58	9.36	0.035	54.92
c_{650} vs. chl-a	$Ax + B$	2.302	−0.046	205	0.26	0.88	14.23	0.097	392.47
	Ax^B	9.408	1.744	205	0.54	0.69	11.23	0.077	357.81
ECO-FL vs. POC	$Ax + B$	57.719	22.441	194	0.68	34.75	8.50	9.47	34.39
	Ax^B	80.730	0.328	194	0.48	44.20	10.81	10.0	38.82
c_{650} vs. POC	$Ax + B$	390.67	11.6125	183	0.64	37.91	9.47	8.13	35.37
	Ax^B	253.95	0.674	183	0.56	41.59	10.40	9.04	37.30

Sea are of Atlantic origin similar to the waters south, west and north of Svalbard (Makarewicz et al., 2018), but are very different from near-coastal and Polar Waters, in e.g. western Fram Strait and the Transpolar drift, which carry a significantly higher CDOM load from Arctic rivers (e.g. Pavlov et al., 2015; Granskog et al., 2012). This means the largest impact on the variation in absorption and scattering properties are due to organic particulate matter.

South of the Polar Front, we observed wind-driven mixing of phytoplankton down to 200 m in early May. To our knowledge, such strong vertical wind-mixing of phytoplankton has rarely been observed, but mixing down to 150 m was observed further south in the Barents Sea in May 1999 (Reigstad et al., 2002). Here, the downwelling also coincided with the Polar Front, which has also been predicted by numerical modeling of the area (Le Fouest et al., 2011). However, the coupling between wind events, sea ice and the Polar Front in relation to vertical mixing has not been studied in great detail, and episodic downwelling events could play a key role in the regional biological carbon pump of the region (Rogge et al., 2023). During the summer months, a distinct surface and subsurface bloom is limited vertically by sea ice melt-induced stratification (Koenig et al.). The level of surface stratification is a key environmental factor for polar marine ecosystems that is likely to change in a future Barents Sea with less sea ice, and needs to be studied in more detail with mesoscale biogeochemical modeling (Ingvaldsen et al., 2021).

We also observed significant particle resuspension in the bottom boundary layer throughout the northwestern shelf, often affecting water masses more than 50 m above the ocean floor. This is similar to the observations in the adjacent Storfjorden (Petit et al., 2022), albeit the mechanism is likely different. While in Storfjorden this appears to be caused by density currents driven by sea-ice formation, here it indicates that there may be substantial turbulent interactions between the ocean floor and the pelagic water masses, which could contribute to replenishing nutrients during the stormy and less stratified autumn and winter seasons. The increased light attenuation near the bottom also

means lower visibility, making it a possible sanctuary for prey hiding from visual predators.

Investigating physical drivers means coupling factors that could influence the absorption and scattering properties. This allows us to link *what is in the water* with *how much light is in the water*, which is especially important in the Arctic where light is a key limiting factor for large parts of the ecosystem. Robust and accurate bio-optical models would greatly improve biogeochemical and ecological ocean models, which currently use highly simplified parametrizations of the underwater light field (e.g. Ljungström et al., 2021; Yumruktepe et al., 2022). Such bio-optical models could also yield good proxy relationships with biogeochemical properties which are resource-demanding to measure, such as POC or DOC, which is relevant in observing the biological carbon pump.

Estimates of the underwater light field have not been included in this study for brevity, given that extensive radiative transfer modeling is required to estimate the combined effects of snow, sea ice, and cloud properties across several seasons in addition to the variable bio-optical properties of the water column. This is a topic of future studies. The use of a single-parameter diffuse attenuation coefficient has significant problems, as is the use of the traditional euphotic depth (e.g. 1% of surface irradiance) at high latitudes, since the incoming light distribution at the surface varies drastically with time of the year (Lee et al., 2005; Kaartvedt et al., 2019; Ardyna et al., 2020). However, considerable progress in underwater light modeling of Arctic waters has been made in recent years, which will help advance our understanding of light as an ecological driver (Connan-McGinty et al., 2022; Lebrun et al., 2023).

What are the knowledge gaps for bio-optical relationships in the northern Barents Sea? Our findings suggests that a regional, or even seasonal model for absorption due to chlorophyll-a is needed, since using the global relationship leads to an overestimation of the particulate absorption. Moreover, different studies in the ice-covered Arctic Ocean show divergent results for the same relationship, suggesting that chlorophyll-specific absorption may also vary depending on season or species composition. For instance, Kostakis et al. (2020) showed that the global relationship provided reasonable agreement during a relatively ice-free year in the Barents Sea, which implies that the differences could be due to light adaptation by under-ice phytoplankton, or through ice algae influence. POC may turn out to be a more robust predictor of optical properties in ice-covered surface waters than chlorophyll. Beam attenuation at 650 nm was found to be a useful proxy measurement for POC over many seasons, which can yield high-resolved measurements and improvements in our biogeochemical observational capabilities. Adaptive algorithms for estimating POC from scattering and fluorescence measurements have recently been developed (Koestner et al., 2022), suggesting that POC estimates from CTD data may be further improved in the future.

Declaration of competing interest

The authors declare that they have no known competing financial interests or personal relationships that could have appeared to influence the work reported in this paper.

Data availability

The hydrographic data from the ship-based CTD have been published in Gerland (2022), Ludvigsen (2022), Jones (2022), Chlorophyll-*a* data in Vader (2022), and POC data in Marquardt et al. (2022a,b,c)

The optical data from measurements of CDOM and particulate matter absorption are available from Sandven et al. (2023a,b). Furthermore, the *in situ* absorption and attenuation data is found in Sandven et al. (2023c,d).

Acknowledgments

The authors are grateful for the excellent support at sea by the captain and the crew of *R/V Kronprins Haakon* during the Nansen Legacy expeditions in 2021. Special thanks to Miriam Marquardt and Anna Vader and their teams for producing the POC and chlorophyll data, and to Adam Steer and Dmitry Divine for their help with the sea ice concentration data.

Funding

This work was funded by the Research Council of Norway through the project *The Nansen Legacy* (Grant No. 276730). MAG received funding from the European Union's Horizon 2020 research and innovation programme (grant agreement No 101003826) via the project *CRiceS* (Climate Relevant interactions and feedbacks: the key role of sea ice and Snow in the polar and global climate system).

Appendix. Uncertainty assessment of absorption measurements

Absorption measurements of natural waters are challenging due to the numerous error sources involved. In this study, multiple methods have been used to determine the particulate, CDOM and total *in situ* absorption. In Fig. 15, we compare the total non-water absorption computed from water sample measurements with ac-s measurements collected at corresponding depths. Different ac-s scattering corrections are compared, along with the uncorrected signal. For the ac-s absorption meter, the main uncertainties are the scattering error and, when operating close to the sensitivity limit in very clear waters, small offsets can have large relative contributions to the signal. Fig. 15A shows clear biases for most scattering corrections, in particular for the May 2021 data set (indicated by dash-dot line). Note that the measured absorption was generally higher in the May 2021 data set than for the March 2021 cruise (solid line), meaning that the bias and uncertainties are relatively lower compared to the measured signal. For the March 2021 data set, the semi-empirical scattering correction was found to give the lowest uncertainty. The standard proportional correction was found to give the best agreement within the May 2021 absorption measurements, and was used for the entire data set. The agreement between water sample data and the corrected ac-s data in shown in Fig. 14C.

The observed uncertainties are similar to the operational limits of the ac-s in clear waters given by the IOCCG (2018). Furthermore, the scattering corrections are assumed to work on a basin-wide level, but may vary in performance based on water masses and particles. Thus, the development of more robust correction methods would be advantageous for using the ac-s on long transects and highly varying depth profiles. For this reason, water sample measurements of absorption have been primarily used for inferring relationships between absorption and chl-a and POC, while ac-s absorption measurements have limited to the descriptive analysis in Figs. 2 and 3.

Finally, Fig. 14D compares two commonly derived ac-s products, the absorption slope factor and absorption line height at 676 nm, calculated from ac-s and water sample measurements. The spectral slope agrees reasonably well, but has a limited variability. The absorption line height at 676 nm is visibly overestimated by the ac-s when compared to the water sample estimates. This could be due to differences in spectral response, but potentially also uncertainties due to the filter pad amplification factor. The line height is not particularly affected by the scattering error.

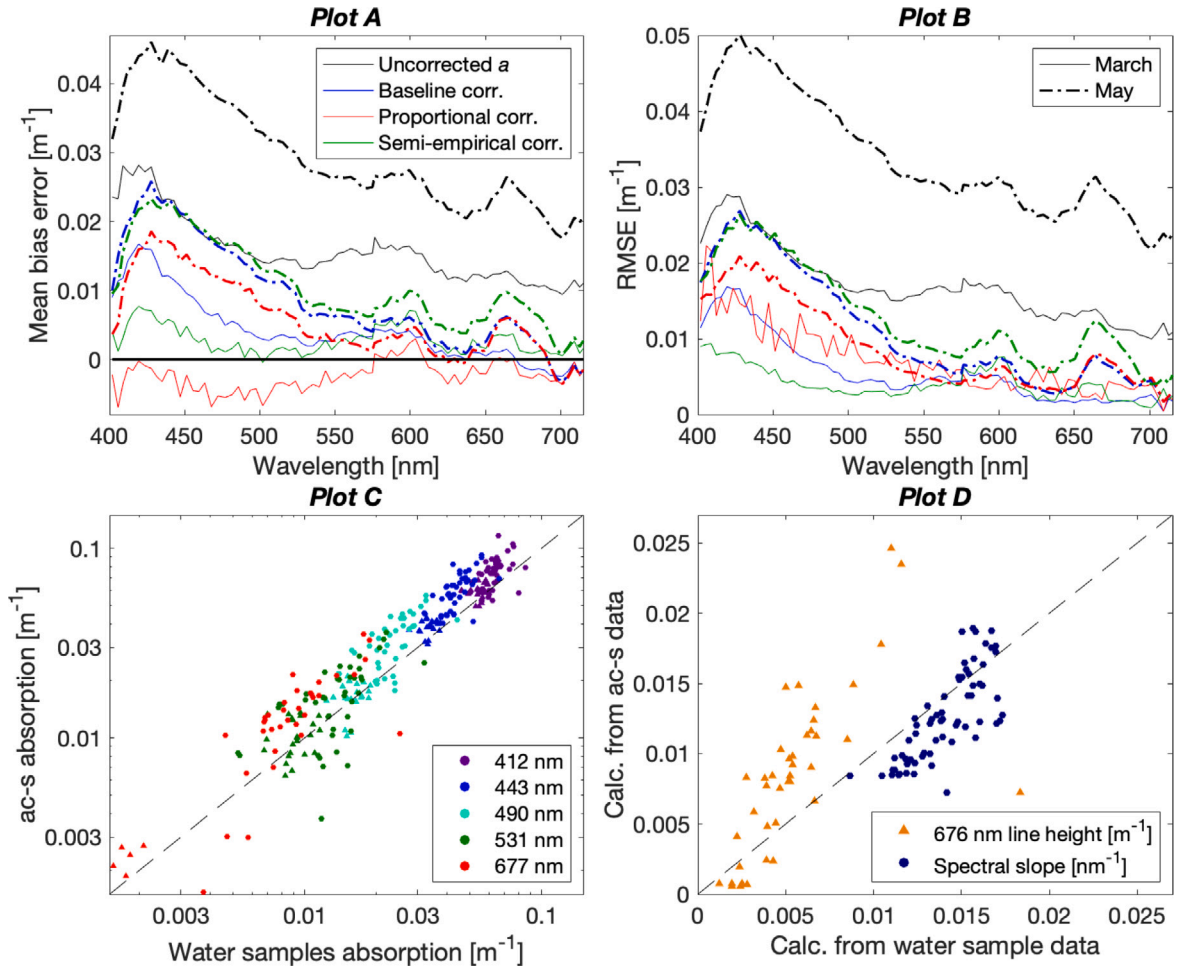

Fig. 15. Uncertainty plots for the ac-s absorption measurements.

References

Aas, E., Berge, G., 1976. Irradiance observations in the Norwegian and Barents Seas. In: Institute Report Series (Universitetet I Oslo. Institutt for Geofysikk). Department of Geophysics, University of Oslo, Retrieved from http://urn.nb.no/URN:NBN:no-64216.

Aas, E., Høkedal, J., 1996. Penetration of ultraviolet B, blue and quanta irradiance into Svalbard waters. Polar Res. 15 (2), 127–138. http://dx.doi.org/10.1111/j.1751-8369.1996.tb00464.x.

Ardyna, M., Mundy, C., Mayot, N., Matthes, L.C., Oziel, L., Horvat, C., Leu, E., Assmy, P., Hill, V., Matrai, P.A., Gale, M., Melnikov, I.A., Arrigo, K.R., 2020. Under-ice phytoplankton blooms: Shedding light on the "invisible" part of Arctic primary production. Front. Mar. Sci. 7, 608032. http://dx.doi.org/10.3389/fmars.2020.608032.

Assmy, P., Fernández-Méndez, M., Duarte, P., Meyer, A., Randelhoff, A., Mundy, C.J., Olsen, L.M., Kauko, H.M., Bailey, A., Chierici, M., Cohen, L., Doulgeris, A.P., Ehn, J.K., Fransson, A., Gerland, S., Hop, H., Hudson, S.R., Hughes, N., Itkin, P., Johnsen, G., King, J.A., Koch, B.P., Koenig, Z., Kwasniewski, S., Laney, S.R., Nicolaus, M., Pavlov, A.K., Polashenski, C.M., Provost, C., Rösel, A., Sandbu, M., Spreen, G., Smedsrud, L.H., Sundfjord, A., Taskjelle, T., Tatarek, A., Wiktor, J., Wagner, P.M., Wold, A., Steen, H., Granskog, M.A., 2017. Leads in Arctic pack ice enable early phytoplankton blooms below snow-covered sea ice. Sci. Rep. 7 (1), 40850. http://dx.doi.org/10.1038/srep40850.

Bailey, H., Hubbard, A., Klein, E.S., Mustonen, K.-R., Akers, P.D., Marttila, H., Welker, J.M., 2021. Arctic sea-ice loss fuels extreme European snowfall. Nat. Geosci. 14 (5), 283–288. http://dx.doi.org/10.1038/s41561-021-00719-y.

Bartsch, I., Paar, M., Fredriksen, S., Schwanitz, M., Daniel, C., Hop, H., Wiencke, C., 2016. Changes in kelp forest biomass and depth distribution in Kongsfjorden, Svalbard, between 1996–1998 and 2012–2014 reflect Arctic warming. Polar Biol. 39, 2021–2036. http://dx.doi.org/10.1007/s00300-015-1870-1.

Behrenfeld, M.J., Boss, E., 2006. Beam attenuation and chlorophyll concentration as alternative optical indices of phytoplankton biomass. J. Mar. Res. 64 (3), 431–451, Retrieved from https://misclab.umeoce.maine.edu/documents/BehrenfeldBoss2006.pdf.

Bélanger, S., Babin, M., Tremblay, J.-É., 2013. Increasing cloudiness in Arctic damps the increase in phytoplankton primary production due to sea ice receding. Biogeosciences 10 (6), 4087–4101. http://dx.doi.org/10.5194/bg-10-4087-2013.

Boss, E., Guidi, L., Richardson, M.J., Stemmann, L., Gardner, W., Bishop, J.K., Anderson, R.F., Sherrell, R.M., 2015. Optical techniques for remote and in-situ characterization of particles pertinent to GEOTRACES. Prog. Oceanogr. 133, 43–54. http://dx.doi.org/10.1016/j.pocean.2014.09.007.

Boss, E., Twardowski, M.S., Herring, S., 2001. Shape of the particulate beam attenuation spectrum and its inversion to obtain the shape of the particulate size distribution. Appl. Opt. 40 (27), 4885–4893. http://dx.doi.org/10.1364/AO.40.004885.

Bricaud, A., Morel, A., Babin, M., Allali, K., Claustre, H., 1998. Variations of light absorption by suspended particles with chlorophyll *a* concentration in oceanic (case 1) waters: Analysis and implications for bio-optical models. J. Geophys. Res.: Oceans 103 (C13), 31033–31044. http://dx.doi.org/10.1029/98JC02712.

Bricaud, A., Stramski, D., 1990. Spectral absorption coefficients of living phytoplankton and nonalgal biogenous matter: A comparison between the Peru upwelling area and the Sargasso Sea. Limnol. Oceanogr. 35 (3), 562–582. http://dx.doi.org/10.4319/lo.1990.35.3.0562.

Castellani, G., Veyssière, G., Karcher, M., Stroeve, J., Banas, S.N., Bouman, A.H., Brierley, S.A., Connan, S., Cottier, F., Große, F., et al., 2022. Shine a light: Under-ice light and its ecological implications in a changing Arctic Ocean. Ambio 51, 307–317. http://dx.doi.org/10.1007/s13280-021-01662-3.

Castro de la Guardia, L., Farinas, T., Marches, C., Amargant Arumí, P., S., B., Assmy, P., Gradinger, R., Duarte, P., this issue. Model and satellite-derived phytoplankton primary production show no long-term trends in the north-western Barents Sea, but uncovered a regime shift induced by a pulse of Atlantic Water. Prog. Oceanogr..

Castro de la Guardia, L., Filbee-Dexter, K., Reimer, J., MacGregor, K.A., Garrido, I., Singh, R.K., Bélanger, S., Konar, B., Iken, K., Johnson, L.E., et al., 2023. Increasing depth distribution of Arctic kelp with increasing number of open water days with light. Elementa 11 (1), http://dx.doi.org/10.1525/elementa.2022.00051.

Cohen, J.H., Berge, J., Moline, M.A., Sørensen, A.J., Last, K., Falk-Petersen, S., Renaud, P.E., Leu, E.S., Grenvald, J., Cottier, F., et al., 2015. Is ambient light during the high Arctic polar night sufficient to act as a visual cue for zooplankton? PLoS One 10 (6), e0126247. http://dx.doi.org/10.1371/journal.pone.0126247.

Connan-McGinty, S., Banas, N.S., Berge, J., Cottier, F., Grant, S., Johnsen, G., Kopec, T.P., Porter, M., McKee, D., 2022. Midnight sun to Polar night: A model of seasonal light in the Barents Sea. J. Adv. Modelling Earth Syst. 14 (10), e2022MS003198. http://dx.doi.org/10.1029/2022MS003198.

Dallokken, R., Sandvik, R., Sakshaug, E., 1994. Variations in bio-optical properties in the Greenland/Iceland/Norwegian Seas. In: Ocean Optics XII, Vol. 2258. SPIE, pp. 266–276. http://dx.doi.org/10.1117/12.190070.

Erga, S.R., Ssebiyonga, N., Hamre, B., Frette, Ø., Rey, F., Drinkwater, K., 2014. Nutrients and phytoplankton biomass distribution and activity at the Barents Sea Polar Front during summer near Hopen and Storbanken. J. Mar. Syst. 130, 181–192. http://dx.doi.org/10.1016/j.jmarsys.2012.12.008.

Falk-Petersen, S., Hop, H., Budgell, W.P., Hegseth, E.N., Korsnes, R., Løyning, T.B., Ørbæk, J.B., Kawamura, T., Shirasawa, K., 2000. Physical and ecological processes in the marginal ice zone of the northern Barents Sea during the summer melt period. J. Mar. Syst. 27 (1–3), 131–159. http://dx.doi.org/10.1016/S0924-7963(00)00064-6.

Gardner, W.D., Richardson, M.J., Mishonov, A.V., Lam, P.J., Xiang, Y., 2022. Distribution, sources, and dynamics of particulate matter along Trans-Arctic sections. J. Geophys. Res.: Oceans 127 (6), e2021JC017970. http://dx.doi.org/10.1029/2021JC017970.

Gerland, S., 2022. CTD data from Nansen Legacy Cruise - Seasonal cruise Q1. http://dx.doi.org/10.21335/NMDC-1491279668.

Gerland, S., Wold, A., Altuna, N.E., Anglada-Ortiz, G., Arumi, M.A., Yasemin, B., Bratrein, M., Chitkara, C., de Freitas, T.R., Divine, D., Dybdahl, J., Espinel, N., Flo, S., Gawinski, C., Giebichestein, J., Grytaas, J.A., Jones, E., Jorda, E., Jortveit, A., Karlsson, J., Keck, A., Khuong, D., Kline, S., Kohler, S., Kull, L., Marquardt, M., Müller, O., Nowicki, R., Palmesen, M., Petit, T., Pitusi, V., Sen, A., Steer, A., Steinsland, A., Summers, N., Ziegler, A., 2022. Seasonal cruise Q1 2021: Cruise report. In: The Nansen Legacy Report Series (29). http://dx.doi.org/10.7557/nlrs.6464.

Goncalves-Araujo, R., Rabe, B., Peeken, I., Bracher, A., 2018. High colored dissolved organic matter (CDOM) absorption in surface waters of the central-eastern Arctic Ocean: Implications for biogeochemistry and ocean color algorithms. PLoS One 13 (1), e0190838. http://dx.doi.org/10.1371/journal.pone.0190838.

Gosselin, M., Levasseur, M., Wheeler, P.A., Horner, R.A., Booth, B.C., 1997. New measurements of phytoplankton and ice algal production in the Arctic Ocean. Deep Sea Res. II: Top. Stud. Oceanogr. 44 (8), 1623–1644. http://dx.doi.org/10.1016/S0967-0645(97)00054-4.

Graham, R.M., Itkin, P., Meyer, A., Sundfjord, A., Spreen, G., Smedsrud, L.H., Liston, G.E., Cheng, B., Cohen, L., Divine, D., et al., 2019. Winter storms accelerate the demise of sea ice in the Atlantic sector of the Arctic Ocean. Sci. Rep. 9 (1), 1–16. http://dx.doi.org/10.1038/s41598-019-45574-5.

Granskog, M.A., Pavlov, A.K., Sagan, S., Kowalczuk, P., Raczkowska, A., Stedmon, C.A., 2015. Effect of sea-ice melt on inherent optical properties and vertical distribution of solar radiant heating in Arctic surface waters. J. Geophys. Res.: Oceans 120 (10), 7028–7039. http://dx.doi.org/10.1002/2015JC011087.

Granskog, M.A., Stedmon, C.A., Dodd, P.A., Amon, R.M., Pavlov, A.K., de Steur, L., Hansen, E., 2012. Characteristics of colored dissolved organic matter (CDOM) in the Arctic outflow in the Fram Strait: Assessing the changes and fate of terrigenous CDOM in the Arctic Ocean. J. Geophys. Res.: Oceans 117 (C12), http://dx.doi.org/10.1029/2012JC008075.

Häfker, N.S., Connan-McGinty, S., Hobbs, L., McKee, D., Cohen, J.H., Last, K.S., 2022. Animal behavior is central in shaping the realized diel light niche. Commun. Biol. 5 (1), 562. http://dx.doi.org/10.1038/s42003-022-03472-z.

Hamre, B., Winther, J.-G., Gerland, S., Stamnes, J.J., Stamnes, K., 2004. Modeled and measured optical transmittance of snow-covered first-year sea ice in Kongsfjorden, Svalbard. J. Geophys. Res.: Oceans 109 (C10), http://dx.doi.org/10.1029/2003JC001926.

Hancke, K., Hovland, E.K., Volent, Z., Pettersen, R., Johnsen, G., Moline, M., Sakshaug, E., 2014. Optical properties of CDOM across the polar front in the Barents Sea: Origin, distribution and significance. J. Mar. Syst. 130, 219–227. http://dx.doi.org/10.1016/j.jmarsys.2012.06.006.

Hill, P., Boss, E., Newgard, J., Law, B., Milligan, T., 2011. Observations of the sensitivity of beam attenuation to particle size in a coastal bottom boundary layer. J. Geophys. Res.: Oceans 116 (C2), http://dx.doi.org/10.1029/2010JC006539.

Hoppe, C.J., 2022. Always ready? Primary production of Arctic phytoplankton at the end of the polar night. Limnol. Oceanogr. Lett. 7 (2), 167–174. http://dx.doi.org/10.1002/lol2.10222.

Hovland, E.K., Hancke, K., Alver, M.O., Drinkwater, K., Høkedal, J., Johnsen, G., Moline, M., Sakshaug, E., 2014. Optical impact of an Emiliania huxleyi bloom in the frontal region of the Barents Sea. J. Mar. Syst. 130, 228–240. http://dx.doi.org/10.1016/j.jmarsys.2012.07.002.

Huot, Y., Babin, M., Bruyant, F., Grob, C., Twardowski, M., Claustre, H., 2007. Relationship between photosynthetic parameters and different proxies of phytoplankton biomass in the subtropical ocean. Biogeosciences 4 (5), 853–868. http://dx.doi.org/10.5194/bg-4-853-2007.

Ingvaldsen, R.B., Assmann, K.M., Primicerio, R., Fossheim, M., Polyakov, I.V., Dolgov, A.V., 2021. Physical manifestations and ecological implications of Arctic atlantification. Nature Rev. Earth Environ. 2 (12), 874–889. http://dx.doi.org/10.1038/s43017-021-00228-x.

IOCCG, 2018. Inherent optical property measurements and protocols: Absorption coefficient. In: IOCCG Ocean Optics and Biogeochemistry Protocols for Satellite Ocean Colour Sensor Validation, Vol. 1. http://dx.doi.org/10.25607/OBP-119.

Isaksen, K., Nordli, Ø., Ivanov, B., Køltzow, M.A., Aaboe, S., Gjelten, H.M., Mezghani, A., Eastwood, S., Førland, E., Benestad, R.E., et al., 2022. Exceptional warming over the Barents area. Sci. Rep. 12 (1), 1–18. http://dx.doi.org/10.1038/s41598-022-13568-5.

Jones, E., 2022. CTD data from Nansen Legacy Cruise - Joint Cruise 2-1. http://dx.doi.org/10.21335/NMDC-2085836005.

Jones, E., Reigstad, M., Velasco, N.E., Gjerland, A., Goraguer, L., Lødemel, H.H., Kline, S., Lind, S., Marsden, L., Maurstad, M., et al., 2022. JC2-1 joint cruise part 1 2021: Cruise report. In: The Nansen Legacy Report Series (35). http://dx.doi.org/10.7557/nlrs.6744.

Kaartvedt, S., Langbehn, T.J., Aksnes, D.L., 2019. Enlightening the ocean's twilight zone. ICES J. Mar. Sci. 76 (4), 803–812. http://dx.doi.org/10.1093/icesjms/fsz010.

Koenig, Z., Lundesgaard, O., Muilwijk, M., Sandven, H., Granskog, M.A., Assmy, P., Assmann, K., Chierici, M., Fransson, A., Gerland, S., Jones, E., Renner, A.H.H., Lind, S., this issue. From winter to late summer in the northwestern Barents Sea shelf: Sea ice and upper ocean evolution and impacts on nutrient and phytoplankton dynamics. Prog. Oceanogr..

Koestner, D., Stramski, D., Reynolds, R.A., 2022. A multivariable empirical algorithm for estimating particulate organic carbon concentration in marine environments from optical backscattering and chlorophyll-a measurements. Front. Mar. Sci. 9, http://dx.doi.org/10.3389/fmars.2022.941950.

Kogeler, J., Rey, F., 1999. Ocean colour and the spatial and seasonal distribution of phytoplankton in the Barents Sea. Int. J. Remote Sens. 20 (7), 1303–1318. http://dx.doi.org/10.1080/014311699212740.

Kostakis, I., Röttgers, R., Orkney, A., Bouman, H.A., Porter, M., Cottier, F., Berge, J., McKee, D., 2020. Development of a bio-optical model for the Barents Sea to quantitatively link glider and satellite observations. Phil. Trans. R. Soc. A 378 (2181), 20190367. http://dx.doi.org/10.1098/rsta.2019.0367.

Kostakis, I., Twardowski, M., Roesler, C., Röttgers, R., Stramski, D., McKee, D., Tonizzo, A., Drapeau, S., 2021. Hyperspectral optical absorption closure experiment in complex coastal waters. Limnol. Oceanogr.: Methods 19 (9), 589–625. http://dx.doi.org/10.1002/lom3.10447.

Le Fouest, V., Postlethwaite, C., Maqueda, M.A.M., Belanger, S., Babin, M., 2011. On the role of tides and strong wind events in promoting summer primary production in the Barents Sea. Cont. Shelf Res. 31 (17), 1869–1879. http://dx.doi.org/10.1016/j.csr.2011.08.013.

Lebrun, M., Vancoppenolle, M., Madec, G., Babin, M., Becu, G., Lourenço, A., Nomura, D., Vivier, F., Delille, B., 2023. Light under Arctic sea ice in observations and earth system models. J. Geophys. Res.: Oceans e2021JC018161. http://dx.doi.org/10.1029/2021JC018161.

Lee, Z.-P., Du, K.-P., Arnone, R., 2005. A model for the diffuse attenuation coefficient of downwelling irradiance. J. Geophys. Res.: Oceans 110 (C2), http://dx.doi.org/10.1029/2004JC002573.

Lefering, I., Röttgers, R., Utschig, C., McKee, D., 2017. Uncertainty budgets for liquid waveguide CDOM absorption measurements. Appl. Opt. 56 (22), 6357–6366. http://dx.doi.org/10.1364/AO.56.006357.

Lefering, I., Röttgers, R., Weeks, R., Connor, D., Utschig, C., Heymann, K., McKee, D., 2016. Improved determination of particulate absorption from combined filter pad and PSICAM measurements. Opt. Express 24 (22), 24805–24823. http://dx.doi.org/10.1364/OE.24.024805.

Leu, E., Mundy, C., Assmy, P., Campbell, K., Gabrielsen, T., Gosselin, M., Juul-Pedersen, T., Gradinger, R., 2015. Arctic spring awakening – steering principles behind the phenology of vernal ice algal blooms. Prog. Oceanogr. 139, 151–170. http://dx.doi.org/10.1016/j.pocean.2015.07.012.

Lind, S., Ingvaldsen, R.B., Furevik, T., 2018. Arctic warming hotspot in the northern Barents sea linked to declining sea-ice import. Nature Clim. Change 8, 634–639. http://dx.doi.org/10.1038/s41558-018-0205-y.

Ljungström, G., Langbehn, T.J., Jørgensen, C., 2021. Light and energetics at seasonal extremes limit poleward range shifts. Nature Clim. Change 11 (6), 530–536. http://dx.doi.org/10.1038/s41558-021-01045-2.

Lokhov, A., Kravchishina, M., Klyuvitkin, A., Kochenkova, A., 2020. In situ measurements of the characteristics of suspended particles in the Barents Sea by the LISST-deep laser diffractometer. Oceanology 60, 650–663. http://dx.doi.org/10.1134/S0001437020050148.

Ludvigsen, M., 2022. CTD data from Nansen Legacy Cruise - Seasonal cruise Q2. http://dx.doi.org/10.21335/NMDC-515075317.

Ludvigsen, M., Assmy, P., Adams, M.J.S., Amargant-Arumí, M., Mo-Bjørkelund, T., Bodur, Y., Bremnes, J.E., Flo, S., Gawinski, C., Giebichtenstein, J., Halvorsen, E., Hatlebakk, M., Hess, S., Hop, H., Itkin, P., Jones, E., Karlsson, K., Keck, A., Kohlbach, D., Kohler, S.G., Krapp, R., Leopold, P., Marquardt, M., Molina, E.J., Nowicki, R., Olsen, L.M., Ortiz, G.A., Petit, T., de Freitas, T.R., Saubrekka, K., Sen, A., Steer, A., Summers, N., Thiele, S., Thorstensen, H., Vihtakari, M., 2022. Seasonal cruise Q2 2021: Cruise report. In: The Nansen Legacy Report Series (34). http://dx.doi.org/10.7557/nlrs.6689.

Lundesgaard, Ø., Sundfjord, A., Lind, S., Nilsen, F., Renner, A.H., 2022. Import of Atlantic water and sea ice controls the ocean environment in the northern Barents Sea. Ocean Sci. 18 (5), 1389–1418. http://dx.doi.org/10.5194/os-18-1389-2022.

Makarewicz, A., Kowalczuk, P., Sagan, S., Granskog, M.A., Pavlov, A.K., Zdun, A., Borzycka, K., Zabłocka, M., 2018. Characteristics of chromophoric and fluorescent dissolved organic matter in the Nordic Seas. Ocean Sci. 14, 543–562. http://dx.doi.org/10.5194/os-14-543-2018.

Mannino, A., Russ, M.E., Hooker, S.B., 2008. Algorithm development and validation for satellite-derived distributions of DOC and CDOM in the US middle Atlantic bight. J. Geophys. Res.: Oceans 113 (C7), http://dx.doi.org/10.1029/2007JC004493.

Marquardt, M., Bodur, Y.V., Dubourg, P., Reigstad, M., 2022a. Concentration of particulate organic carbon (POC) and particulate organic nitrogen (PON) from the sea water and sea ice in the northern Barents Sea as part of the Nansen Legacy project, Cruise 2021703, Q1. http://dx.doi.org/10.11582/2022.00053.

Marquardt, M., Bodur, Y.V., Dubourg, P., Reigstad, M., 2022b. Concentration of particulate organic carbon (POC) and particulate organic nitrogen (PON) from the sea water and sea ice in the northern Barents Sea as part of the Nansen Legacy project, Cruise 2021704, Q2. http://dx.doi.org/10.11582/2022.00054.

Marquardt, M., Goraguer, L., Duborg, P., Reigstad, M., 2022c. Concentration of particulate organic carbon (POC) and particulate organic nitrogen (PON) from the sea water and sea ice in the northern Barents Sea as part of the Nansen Legacy project, Cruise 2021708, JC2-1. http://dx.doi.org/10.11582/2022.00050.

Mobley, C.D., 1994. Light and Water: Radiative Transfer in Natural Waters. Academic Press.

Moore, C.C., Bruce, E.J., Pegau, W.S., Weidemann, A.D., 1997. WET labs ac-9: Field calibration protocol, deployment techniques, data processing, and design improvements. In: Ocean Optics XIII, Vol. 2963. SPIE, pp. 725–730. http://dx.doi.org/10.1117/12.266391.

Neukermans, G., Loisel, H., Mériaux, X., Astoreca, R., McKee, D., 2012. In situ variability of mass-specific beam attenuation and backscattering of marine particles with respect to particle size, density, and composition. Limnol. Oceanogr. 57 (1), 124–144. http://dx.doi.org/10.4319/lo.2012.57.1.0124.

Neukermans, G., Reynolds, R.A., Stramski, D., 2014. Contrasting inherent optical properties and particle characteristics between an under-ice phytoplankton bloom and open water in the Chukchi Sea. Deep Sea Res. II: Top. Stud. Oceanogr. 105, 59–73. http://dx.doi.org/10.1016/j.dsr2.2014.03.014.

Nicolaus, M., Katlein, C., Maslanik, J., Hendricks, S., 2012. Changes in Arctic sea ice result in increasing light transmittance and absorption. Geophys. Res. Lett. 39, L24501. http://dx.doi.org/10.1029/2012GL053738.

Omand, M.M., Steinberg, D.K., Stamieszkin, K., 2021. Cloud shadows drive vertical migrations of deep-dwelling marine life. Proc. Natl. Acad. Sci. 118 (32), e2022977118. http://dx.doi.org/10.1073/pnas.2022977118.

Onarheim, I.H., Årthun, M., 2017. Toward an ice-free Barents Sea. Geophys. Res. Lett. 44 (16), 8387–8395. http://dx.doi.org/10.1002/2017GL074304.

Organelli, E., Dall'Olmo, G., Brewin, R.J., Nencioli, F., Tarran, G.A., 2020. Drivers of spectral optical scattering by particles in the upper 500 m of the Atlantic Ocean. Opt. Express 28 (23), 34147–34166. http://dx.doi.org/10.1364/OE.408439.

Oziel, L., Neukermans, G., Ardyna, M., Lancelot, C., Tison, J.-L., Wassmann, P., Sirven, J., Ruiz-Pino, D., Gascard, J.-C., 2017. Role for Atlantic inflows and sea ice loss on shifting phytoplankton blooms in the Barents Sea. J. Geophys. Res.: Oceans 122 (6), 5121–5139. http://dx.doi.org/10.1002/2016JC012582.

Pavlov, A.K., Granskog, M.A., Stedmon, C.A., Ivanov, B.V., Hudson, S.R., Falk-Petersen, S., 2015. Contrasting optical properties of surface waters across the Fram Strait and its potential biological implications. J. Mar. Syst. 143, 62–72. http://dx.doi.org/10.1016/j.jmarsys.2014.11.001.

Pavlov, A.K., Taskjelle, T., Kauko, H.M., Hamre, B., Hudson, S.R., Assmy, P., Duarte, P., Fernández-Méndez, M., Mundy, C., Granskog, M.A., 2017. Altered inherent optical properties and estimates of the underwater light field during an Arctic under-ice bloom of Phaeocystis pouchetii. J. Geophys. Res.: Oceans 122 (6), 4939–4961. http://dx.doi.org/10.1002/2016JC012471.

Petit, T., Hamre, B., Sandven, H., Röttgers, R., Kowalczuk, P., Zablocka, M., Granskog, M.A., 2022. Inherent optical properties of dissolved and particulate matter in an Arctic fjord (Storfjorden, Svalbard) in early summer. Ocean Sci. 18 (2), 455–468. http://dx.doi.org/10.5194/os-18-455-2022.

Rantanen, M., Karpechko, A.Y., Lipponen, A., Nordling, K., Hyvärinen, O., Ruosteenoja, K., Vihma, T., Laaksonen, A., 2022. The Arctic has warmed nearly four times faster than the globe since 1979. Commun. Earth Environ. 3 (1), 168. http://dx.doi.org/10.1038/s43247-022-00498-3.

Rasse, R., Dall'Olmo, G., Graff, J., Westberry, T.K., van Dongen-Vogels, V., Behrenfeld, M.J., 2017. Evaluating optical proxies of particulate organic carbon across the surface Atlantic Ocean. Front. Mar. Sci. 4, 367. http://dx.doi.org/10.3389/fmars.2017.00367.

Raven, J.A., Kübler, J.E., Beardall, J., 2000. Put out the light, and then put out the light. J. Mar. Biol. Assoc. UK 80 (1), 1–25. http://dx.doi.org/10.1017/S0025315499001526.

Reigstad, M., Riser, C.W., Wassmann, P., Ratkova, T., 2008. Vertical export of particulate organic carbon: attenuation, composition and loss rates in the northern Barents Sea. Deep Sea Res. II: Top. Stud. Oceanogr. 55 (20–21), 2308–2319. http://dx.doi.org/10.1016/j.dsr2.2008.05.007.

Reigstad, M., Wassmann, P., Riser, C.W., Øygarden, S., Rey, F., 2002. Variations in hydrography, nutrients and chlorophyll a in the marginal ice-zone and the central Barents Sea. J. Mar. Syst. 38 (1–2), 9–29. http://dx.doi.org/10.1016/S0924-7963(02)00167-7.

Roesler, C.S., Barnard, A.H., 2013. Optical proxy for phytoplankton biomass in the absence of photophysiology: Rethinking the absorption line height. Methods Oceanogr. 7, 79–94. http://dx.doi.org/10.1016/j.mio.2013.12.003.

Roesler, C.S., Uitz, J., Claustre, H., Boss, E., Xing, X., Organelli, E., Briggs, N., Bricaud, A., Schmechtig, C., Poteau, A., D'Ortenzio, J., Drapeau, S., Hantjens, N., Barbieux, M., 2017. Recommendations for obtaining unbiased chlorophyll estimates from in situ chlorophyll fluorometers: A global analysis of WET labs ECO sensors. Limnol. Oceanogr.: Methods 15 (6), 572–585. http://dx.doi.org/10.1002/lom3.10185.

Rogge, A., Janout, M., Loginova, N., Trudnowska, E., Hörstmann, C., Wekerle, C., Oziel, L., Schourup-Kristensen, V., Ruiz-Castillo, E., Schulz, K., et al., 2023. Carbon dioxide sink in the Arctic Ocean from cross-shelf transport of dense Barents Sea water. Nat. Geosci. 16 (1), 82–88. http://dx.doi.org/10.1038/s41561-022-01069-z.

Röttgers, R., Doxaran, D., Dupouy, C., 2016. Quantitative filter technique measurements of spectral light absorption by aquatic particles using a portable integrating cavity absorption meter (QFT-ICAM). Opt. Express 24 (2), A1–A20. http://dx.doi.org/10.1364/OE.24.0000A1.

Röttgers, R., Gehnke, S., 2012. Measurement of light absorption by aquatic particles: improvement of the quantitative filter technique by use of an integrating sphere approach. Appl. Opt. 51 (9), 1336–1351. http://dx.doi.org/10.1364/AO.51.001336.

Röttgers, R., McKee, D., Utschig, C., 2014. Temperature and salinity correction coefficients for light absorption by water in the visible to infrared spectral region. Opt. Express 22 (21), 25093–25108. http://dx.doi.org/10.1364/OE.22.025093.

Röttgers, R., McKee, D., Woźniak, S.B., 2013. Evaluation of scatter corrections for ac-9 absorption measurements in coastal waters. Methods Oceanogr. 7, 21–39. http://dx.doi.org/10.1016/j.mio.2013.11.001.

Sandven, H., Granskog, M., Petit, T., Röttgers, R., Hamre, B., 2023a. CDOM and particulate absorption coefficients of sea water in the northern Barents Sea: Nansen Legacy Cruise Q1 (2021703). Norwegian Polar Institute, http://dx.doi.org/10.21334/npolar.2023.94be39d0.

Sandven, H., Granskog, M., Petit, T., Röttgers, R., Hamre, B., 2023b. CDOM and particulate absorption coefficients of sea water in the northern Barents Sea: Nansen Legacy Cruise Q2 (2021704). Norwegian Polar Institute, http://dx.doi.org/10.21334/npolar.2023.9769a8b4.

Sandven, H., Granskog, M., Petit, T., Röttgers, R., Hamre, B., 2023c. In situ spectral beam attenuation and absorption coefficients of sea water in the northern Barents Sea: Nansen Legacy Cruise Q1 (2021703). Norwegian Polar Institute, http://dx.doi.org/10.21334/npolar.2023.38808452.

Sandven, H., Granskog, M., Petit, T., Röttgers, R., Hamre, B., 2023d. In situ spectral beam attenuation and absorption coefficients of sea water in the northern Barents Sea: Nansen Legacy Cruise Q2 (2021704). Norwegian Polar Institute, http://dx.doi.org/10.21334/npolar.2023.71e9f1e8.

Siegel, D., Doney, S., Yoder, J., 2002. The north Atlantic spring phytoplankton bloom and sverdrup's critical depth hypothesis. Science 296 (5568), 730–733. http://dx.doi.org/10.1126/science.1069174.

Silva, E., Counillon, F., Brajard, J., Korosov, A., Pettersson, L.H., Samuelsen, A., Keenlyside, N., 2021. Twenty-one years of phytoplankton bloom phenology in the Barents, Norwegian, and North Seas. Front. Mar. Sci. 1626. http://dx.doi.org/10.3389/fmars.2021.746327.

Slade, W.H., Boss, E., 2015. Spectral attenuation and backscattering as indicators of average particle size. Appl. Opt. 54 (24), 7264–7277. http://dx.doi.org/10.1364/ao.54.007264.

Stedmon, C., Markager, S., 2001. The optics of chromophoric dissolved organic matter (CDOM) in the Greenland sea: An algorithm for differentiation between marine and terrestrially derived organic matter. Limnol. Oceanogr. 46 (8), 2087–2093. http://dx.doi.org/10.4319/lo.2001.46.8.2087.

Stramski, D., Reynolds, R.A., Kaczmarek, S., Uitz, J., Zheng, G., 2015. Correction of pathlength amplification in the filter-pad technique for measurements of particulate absorption coefficient in the visible spectral region. Appl. Opt. 54 (22), 6763–6782. http://dx.doi.org/10.1364/AO.54.006763.

Sumata, H., de Steur, L., Divine, D.V., Granskog, M.A., Gerland, S., 2023. Regime shift in Arctic ocean sea ice thickness. Nature 615 (7952), 443–449. http://dx.doi.org/10.1038/s41586-022-05686-x.

The Nansen Legacy, 2022. The Nansen Legacy Sampling Protocols: Version 10. The Nansen Legacy Report Series (32). http://dx.doi.org/10.7557/nlrs.6684.

Trowbridge, J.H., Lentz, S.J., 2018. The bottom boundary layer. Annu. Rev. Mar. Sci. 10, 397–420. http://dx.doi.org/10.1146/annurev-marine-121916-063351.

Vader, A., 2022. Chlorophyll A and Phaeopigments Nansen Legacy. Norwegian Marine Data Centre, http://dx.doi.org/10.21335/NMDC-1371694848.

von Appen, W.-J., Waite, A.M., Bergmann, M., Bienhold, C., Boebel, O., Bracher, A., Cisewski, B., Hagemann, J., Hoppema, M., Iversen, M.H., et al., 2021. Sea-ice derived meltwater stratification slows the biological carbon pump: Results from continuous observations. Nature Commun. 12 (1), 7309. http://dx.doi.org/10.1038/s41467-021-26943-z.

Wassmann, P., Reigstad, M., Haug, T., Rudels, B., Carroll, M.L., Hop, H., Gabrielsen, G.W., Falk-Petersen, S., Denisenko, S.G., Arashkevich, E., et al., 2006. Food webs and carbon flux in the Barents sea. Prog. Oceanogr. 71 (2–4), 232–287. http://dx.doi.org/10.1016/j.pocean.2006.10.003.

Werdell, P.J., McKinna, L.I., Boss, E., Ackleson, S.G., Craig, S.E., Gregg, W.W., Lee, Z., Maritorena, S., Roesler, C.S., Rousseaux, C.S., et al., 2018. An overview of approaches and challenges for retrieving marine inherent optical properties from ocean color remote sensing. Prog. Oceanogr. 160, 186–212. http://dx.doi.org/10.1016/j.pocean.2018.01.001.

Yumruktepe, V.Ç., Samuelsen, A., Daewel, U., 2022. ECOSMO II (CHL): A marine biogeochemical model for the north Atlantic and the Arctic. Geosci. Model Dev. 15 (9), 3901–3921. http://dx.doi.org/10.5194/gmd-15-3901-2022.